The decadal state of the terrestrial carbon cycle: global retrievals of terrestrial carbon allocation, pools and residence times

The decadal state of the terrestrial carbon cycle: global retrievals of terrestrial carbon allocation, pools and residence times

A. Anthony Bloom[1,2,3], Jean-François Exbrayat[2,3], Ivar van der Velde[4], Liang Feng[2,3], Mathew Williams[2,3]

1. Jet Propulsion Laboratory, California Institute of Technology, Pasadena, CA, USA

2. School of GeoSciences, University of Edinburgh, Edinburgh, UK

3. National Centre for Earth Observation, Edinburgh, UK

4. Wageningen University, Wageningen, The Netherlands

Corresponding author: A. Anthony Bloom (abloom@jpl.nasa.gov)

Biological Sciences: Environmental Sciences

Abstract

The terrestrial carbon cycle is currently the least constrained component of the global carbon budget. Large uncertainties stem from a poor understanding of plant carbon allocation, stocks, residence times and carbon use efficiency. Imposing observational constraints on the terrestrial carbon cycle and its processes is therefore necessary to better understand its current state and to predict its future state. We combine a

diagnostic ecosystem carbon model with satellite observations of leaf area and biomass (where and when available) and soil carbon data to retrieve the first global estimates of carbon cycle state and process variables at a 1°×1° resolution; retrieved variables are independent from the plant functional type and steady-state paradigms. Our results reveal global emergent relationships in the spatial distribution of key carbon cycle states and processes. Live biomass and dead organic carbon residence times exhibit contrasting spatial features (r=0.3). Allocation to structural carbon is highest in the wet tropics (85–88%) in contrast to higher latitudes (73–82%), where allocation shifts towards photosynthetic carbon. Carbon use efficiency is lowest (0.42–0.44) in the wet tropics. We find an emergent global correlation between retrievals of leaf mass per leaf area and leaf lifespan (r=0.64–0.80) that matches independent trait studies. We show that conventional land-cover types cannot adequately describe the spatial variability of key carbon states and processes (multiple correlation median: 0.41). This mismatch has strong implications for the prediction of terrestrial carbon dynamics, which is currently based on globally applied parameters linked to land-cover or plant functional types.

Significance

Quantitative knowledge of terrestrial carbon pathways and processes is fundamental for understanding the biosphere's response to a changing climate. Carbon allocation, stocks and residence times together define the dynamic state of the terrestrial carbon cycle. These quantities are difficult to measure and remain poorly quantified on a global scale.

Here we retrieve global 1°×1° carbon state and process variables by combining a carbon balance model with satellite observations of biomass and leaf area (where and when available) and global soil carbon data. Our results reveal emergent continental-scale patterns and relationships between carbon states and processes. We find conventional land-cover types cannot capture continental-scale variations of retrieved carbon variables: this mismatch has strong implications for terrestrial carbon cycle predictions.

Keywords: carbon cycle, LAI, biomass, soil carbon, model-data fusion, allocation, residence time.

\body

Introduction

The terrestrial carbon (C) cycle remains the least constrained component of the global C budget (1). In contrast to a relatively stable increase of the ocean CO_2 sink from 0.9 Pg C yr^{-1} to 2.7 Pg C yr^{-1} over the past 40 years, terrestrial CO_2 uptake has been found to vary between a net 4.1 Pg C yr^{-1} sink to a 0.4 Pg C yr^{-1} source, and accounts for a majority of the inter-annual variability in atmospheric CO_2 growth. The complex response of terrestrial ecosystem CO_2 exchanges to short- and long-term changes in temperature, water availability, nutrient availability and rising atmospheric CO_2 (2– 6) remain highly uncertain in C cycle model projections (7). As a result, there are large gaps in our

67 understanding of terrestrial C dynamics, including the magnitude and residence times of
68 the major ecosystem C pools (8, 9) and rates of autotrophic respiration (10). Moreover,
69 the impact of climatic extremes on C cycling, such as recent Amazon droughts (11),
70 highlights the importance of understanding the terrestrial C cycle sensitivity to climate
71 variability. To understand terrestrial CO_2 exchanges in the past, present and future, we
72 need to better constrain current dynamics of ecosystem C cycling, from regional to
73 global scales.
74
75 C uptake, allocation, pool stocks, residence times, respiration and disturbance together
76 drive net CO_2 exchanges (12) on sub-daily to millennial timescales; these C state and
77 process variables also determine the temporal sensitivity of the net C balance to climatic
78 variability. For example, global changes in photosynthetic uptake could lead to a rapid
79 response from short-lived C pools (such as foliage, fine roots and litter), or to a
80 prolonged response from the long-lived C pools (such as woody biomass and soil C),
81 with very different outcomes on ecosystem source/sink behavior. Quantitative
82 knowledge of terrestrial C pathways is therefore central to understanding the temporal
83 responses of the major terrestrial C fluxes – including heterotrophic respiration (13),
84 fires (14, 15) and wetland CH_4 emissions (16, 17) – to inter-annual variations in C uptake.
85
86 While C dynamics have been extensively measured and analyzed at site-level (18– 21),
87 the respiration and allocation of fixed C, and its residence time within the major C pools,
88 are difficult and expensive to measure at site level, and remain poorly quantified on

89 global scales. As a result, global terrestrial C cycle models rely on land-cover type
90 specific C cycling parameters – based on spatially pre-assigned plant functional types –
91 to determine C fluxes and C pools (22). Globally spanning C cycle observations can
92 provide a much-needed constraint on the spatial variability and associated dynamics of
93 the terrestrial C cycle. Over the past decade a growing number of datasets have
94 enhanced understanding of the terrestrial C cycle, including global scale canopy
95 dynamics (NASA Moderate Resolution Imaging Spectroradiometer – MODIS leaf area
96 index – LAI – and burned area products), empirically derived global soil C data
97 (Harmonized World Soil Database – HWSD, 23), satellite-based above and below ground
98 biomass maps for the tropics (ABGB, 24, 25), and Greenhouse Gases Observing Satellite
99 (GOSAT) CO_2 and plant fluorescence (26, 27). These spatially and temporally explicit
100 datasets provide an enhanced view of the terrestrial C cycle, and can be used together
101 to retrieve consistent global C state and process variables. Significant efforts in data-
102 driven estimates of the global C fluxes have been made over the past decade. These
103 include estimates based on atmospheric CO_2 concentrations (1, 28, 29); high-resolution
104 global primary production maps (30) based on FLUXNET eddy covariance tower datasets
105 (18); the mean residence time of terrestrial C (31); ecosystem respiration dependence
106 on temperature, based on FLUXNET data (32) and global C cycle data assimilation
107 systems (33).
108
109 Given an increasing number of C cycle observations, what remains an outstanding
110 challenge is to produce a data-consistent analysis of terrestrial C cycling – including

111 retrievals of C fluxes, C pools, autotrophic respiration, allocation fractions and residence
112 times – based on multiple global-scale earth observations and datasets. Current global-
113 scale terrestrial biosphere models, due to their complexity and structures, are ill-
114 equipped to ingest an ever-increasing volume of earth observations to estimate (instead
115 of prescribing) model parameters, based on the currently available observations. To
116 overcome this challenge, we use a model-data fusion (MDF) approach to retrieve
117 terrestrial C state and process variables during the period 2001–10, without invoking
118 plant functional type or steady-state assumptions. We bring together global MODIS LAI,
119 a tropical biomass map (24), a soil C dataset (23), MODIS burned area (34), and a
120 diagnostic ecosystem C balance model (DALEC2, 19, 35) to retrieve C state and process
121 variables by producing a novel data-consistent and spatially explicit analysis of
122 terrestrial C cycling on a global 1°×1° grid (Fig. 1; we henceforth refer to this model-data
123 fusion setup as the CARbon DAta MOdel framework, or CARDAMOM). Specifically, we
124 address the following questions: how is C uptake partitioned between the live biomass
125 pools and respiration? What is the residence time of C within the major ecosystem C
126 pools? How do estimates of C cycle states and processes vary spatially and to what
127 degree do emergent variable patterns match land-cover maps? We use a Markov Chain
128 Monte Carlo MDF algorithm to retrieve C state and process variables – and their
129 associated uncertainty – within each 1°×1° degree grid cell (see Materials and Methods).
130 The MDF approach retrieves the state and process variables that minimize the model
131 mismatch against any available C cycle observations. Therefore, in the absence of extra-

132 tropical biomass data or winter-time MODIS LAI observations, estimates of 2001–10 C
133 cycle state and process variables are achievable, albeit more uncertain.
134
135 **Results**
136
137 Distinct C allocation patterns emerge from our terrestrial C analysis (Fig. 2). Net primary
138 production (NPP) allocation to structural biomass (wood and fine roots) is largely ≥80%
139 (area-weighted 25^{th} – 75^{th} %ile range = 85–88%) in the wet tropics (<23°N/S; annual
140 precipitation > 1500mm), in contrast to the dry tropics (77–87%), and extra-tropical
141 regions (73–82%). The highest NPP allocations to foliage (≥30%) spatially coincide with
142 major grassland areas, including the North America prairies, Central Asia steppes and
143 the Sahel region in Africa. The dry tropics exhibit relatively high NPP allocation to labile
144 C (7–14%; Fig. S1); this reflects the increasing impact of seasonality on production as
145 precipitation declines, requiring labile C stores for leaf flush. Carbon use efficiency (CUE
146 = 1 - autotrophic respiration fraction) is overall lowest in within the wet tropics (0.42–
147 0.44) in contrast to the dry tropics (0.45–0.50), temperate (23–55°N/S; 0.47–0.50) and
148 high latitudes (>55°N/S; 0.49–0.50).
149
150 Live biomass and dead organic C residence times exhibit contrasting spatial features (r =
151 0.3; Fig. 3). Within the majority of wet tropical land area (56%) – especially across most
152 of the Amazon (76%) and Congo (69%) river basins– the longest C residence time occurs
153 within the woody pool (Fig. S1). In the dry tropics and extra-tropical latitudes, soil C

154 residence times exceed wood C residence time by a median factor of 2.6 (1.6–4.3).
155 Woody residence time is typically shorter in the dry tropics (8–19 yrs) compared to
156 other biomes (wet tropics: 12–21 yrs; temperate: 21–29 yrs; high latitudes: 25–28 yrs).
157 Litter C residence time is typically longer in extra-tropical ecosystems (0.8–1.6 yrs) in
158 comparison to tropical ecosystems (0.4–0.5 yrs). The longest foliar residence time (or
159 leaf lifespan) occurs in the wet tropics and semi-arid regions (Fig. S1).
160
161 Overall, the wet tropics are characterized by relatively high structural C (>100 tC ha^{-1})
162 and photosynthetic C (>2.5 tC ha^{-1})(Fig. 4): in contrast, the dry tropics and extra-tropical
163 regions exhibit less structural and/or photosynthetic C. Foliar C stocks are typically
164 larger in the wet tropics (2.8–4.7 tC ha^{-1}) relative to other biomes (0.2–0.6 tC ha^{-1});
165 similarly, fine root stocks are also greater in the wet tropics (4.0–5.3 tC ha^{-1}), compared
166 to other biomes (0.8–2.7 tC ha^{-1}). Root:shoot (fine root C:leaf C) is lowest in the wet
167 tropics (1.1–1.5), followed by the dry tropics (1.6–1.9) and extra-tropics (1.8–2.1). We
168 find larger woody C uncertainties (1°×1° 90% confidence range / median) in the extra-
169 tropics (1.8-4.6) in contrast to tropical woody C (1.4–1.6) due to the latitudinal limits of
170 the total above- and below-ground biomass map (24). Litter C is greater in high latitudes
171 (2.4–3.4 tC ha^{-1}) relative to temperate (0.6–2.4 tC ha^{-1}) and tropical (0.2–2.6 tC ha^{-1})
172 regions. High-latitude ecosystems have higher labile C stocks linked to seasonal leaf
173 expansion (0.2–0.5 tC ha^{-1}) relative to temperate (0.1–0.3 tC ha^{-1}) and tropical (0.1–0.3
174 tC ha^{-1}) ecosystems.
175

176 We find high leaf C mass per leaf area (LCMA) values in the wet tropics (85-97 gC m^{-2}),
177 and in semi-arid regions, such as the Sahel, South-western United States and the
178 Australian continent (typically >100 gC m^{-2}; Fig. 5); LCMA estimates are lower (typically
179 <80 gC m^{-2}) in high latitudes and the dry tropics. We find a positive correlation between
180 leaf lifespan and LCMA in high-latitude (r = 0.79), temperate (r = 0.80), dry tropical (r =
181 0.78) and wet tropical (r = 0.64) areas.
182
183 Global GPP (global 25^{th} – 75^{th} %ile = 91–134 Pg C yr^{-1}), ecosystem respiration (91–137 Pg
184 C yr^{-1}) and fires (1.3–2.0 Pg C yr^{-1}) are broadly consistent with the MsTMIP terrestrial
185 carbon model ensemble (22), data-driven estimates (36) and bottom-up inventories (37)
186 (Fig. S5). The Net Carbon Exchange uncertainty (-8 to +13 Pg C yr^{-1}) is an order of
187 magnitude greater than mode NCE (-2 Pg C yr^{-1}); NCE latitudinal uncertainty is larger but
188 comparable to the MsTMIP model range. Global atmospheric model CO_2 concentrations
189 based on CARDAMOM mode NCE fluxes are seasonally consistent (r^2 = 0.93, *RMSE* =
190 0.53 ppm CO_2) with mean total column CO_2 measurements (38,Fig. S6). The mean
191 integrated C residence time by (31) is within the range of individual pool residence times
192 at locations B, T, D and W (Fig. 3). The 2001–10 CARDAMOM analysis spatial and
193 temporal LAI variability is consistent with the MODIS LAI constraints (r^2 = 0.8; RMSE =
194 0.6 m^2/m^2). When alternative GPP (36), alternative model structure or biased data
195 constraints (±20%) are imposed at locations B, T, D and W, 88% of median sensitivity
196 analysis estimates are within ±50% of median C state and process variable retrievals
197 (Fig. S2).

198

199 Retrieved C cycle variables are broadly consistent with a range of in-situ measurements
200 (Table S3). Estimates of CUE within the Amazon river basin are comparable to the upper
201 bound of recent measurements (0.32–0.47)(39). Recent estimates of extra-tropical
202 forest C density (40) are on average 38% lower than CARDAMOM total biomass
203 estimates within forested areas (although these are typically within the CARDAMOM
204 1°×1° uncertainty). Estimates of mean Amazon woody C residence times (15–21 yrs) are
205 lower but comparable to above-ground woody C residence times derived from site-level
206 measurements (~20–70 yrs; 20).
207

208 We find that 88-99% of C state and process variability is accounted for by 8 empirical
209 orthogonal basis functions (EOFs, Fig. 6); in other words, retrieved C state and process
210 variables are largely explained by eight modes of spatial variability (Fig. S4). On average,
211 GLOBCOVER land-cover type classifications (41, e.g. deciduous forests, evergreen forests
212 and grasslands) account for <50% of C state and process variability (median multiple
213 correlation coefficient R = 0.41); GLOBCOVER land-cover types best describe spatial
214 variations in C stocks (0.5≤R≤0.8), followed by LCMA (R = 0.4), residence times
215 (0.3≤R≤0.5) and allocation fractions (0.1≤R≤0.4).
216

217 **Discussion**
218

219 Typically C allocation and residence time parameters are based on land-cover types in
220 global-scale terrestrial C cycle studies (9, 22, amongst others); here, spatially broad
221 allocation and residence patterns emerge instead, as a result of the model-data fusion
222 approach. For example, high biomass ecosystems throughout the wet tropics display
223 similar C allocation, residence time and LCMA configurations (Fig. 2–5). Similarly, we
224 find that dead organic matter (DOM) C residence is generally longer in high latitudes
225 (Fig. 3). In comparison to conventional land-cover types, EOFs 1-4 account for a larger
226 degree of the spatial structures in retrieved C variables (Fig. 6); for most variables, the
227 two dominant EOF modes – which together reflect first-order variations in latitude and
228 global precipitation patterns (Fig. S4) – explain more spatial variability than GLOBCOVER
229 land-cover types. The mismatch between land-cover types and retrieved variables has
230 major implications for the estimation and prediction of terrestrial C cycling, which is
231 currently based on small sets of globally applied parameters linked to land-cover types.
232 The importance of climate, biodiversity, fire and anthropogenic disturbance in
233 generating these mismatches needs to be explored in further research (42).
234
235 It also is clear that plant traits vary across biomes (Fig. 2-4, S1), not just at biome
236 boundaries (43), and that there are continental-scale trade-offs and correlations among
237 traits (44). Our analysis is consistent with these viewpoints: for example, the emergent
238 relationship between LCMA (proportional to leaf mass per area) and leaf lifespan (Fig. 5)
239 matches the positive correlation found in global plant trait datasets (45). Evaluating
240 global plant-trait patterns emerging from CARDAMOM provides a novel opportunity for

241 connections to theoretical and functional biodiversity research, and a route to
242 integrating this knowledge into predictive terrestrial C cycle modeling.
243
244 The residence times of major C stocks provide substantial insights into the sensitivity
245 and potential future trajectories of the terrestrial C cycle. For example, land-cover
246 changes in the wet tropics may result in rapid DOM C losses, given the relatively short
247 DOM residence times (<30 yrs) (Fig. 3). In contrast, high-latitude C residence times are
248 an order of magnitude higher (30–300 yrs), and therefore shifts in C allocation or
249 turnover rates are likely to result in long-lived C flux responses. Overall, given the
250 predominant role of C residence times in future terrestrial uptake responses (9), the
251 derived residence times provide a first-order estimate of ecosystem response times as a
252 result of changes in C cycling regimes. However, we note that model structure is likely to
253 be a major source of uncertainty in long-lived (>10yr) C flux predictions. For example,
254 while reduced complexity models can capture some of the principal long-term (>10yr)
255 DOM dynamics represented in earth system models (46) systematic errors in DOM
256 dynamics can arise due to the under-representation of processes controlling DOM
257 residence times (47, 48). We also note that our decadal analysis is unlikely to be able to
258 capture slow feedback processes acting on longer time-scales such as permafrost re-
259 mobilization and priming (49). The large allocation and stocks and short residence time
260 of wood in the wet tropics indicates the potentially rapid potential for regrowth and C
261 accumulation post-disturbance (50). We note that fires are less frequent but major

262 events within boreal ecosystems (51), and therefore longer time-periods are required
263 for retrievals to fully account for the effect of fires on high-latitude C residence times.
264
265 C state and process variable retrievals are sensitive to the uncertainty characteristics of
266 C cycle observations (35) and the prior parameter ranges (Table S1). We highlight that
267 the current coverage and accuracy of C cycle observations (24, 52) remains a major
268 limiting factor in our approach. For example, temperate and high-latitude C stock and
269 residence time uncertainties are higher due to the absence of biomass observations.
270 Undoubtedly, future estimates of globally-spanning biomass density will provide a major
271 constraint on CARDAMOM estimates of extra-tropical C state and process variables (53).
272
273 Land-to-atmosphere C flux estimates could be used to further constrain CARDAMOM C
274 fluxes (Fig. S5) and C cycle variables associated to non-steady C states. For example, soil
275 C residence time samples are negatively correlated with corresponding mean 2001–10
276 NCE samples at locations B (r = -0.3), T (r = -0.4), D (r = -0.5) and W (r = -0.3); therefore,
277 regional- or grid-scale estimates of NCE could provide a much-needed additional
278 constraint on soil C residence time. CARDAMOM flux magnitude and uncertainty can be
279 used as prior information in global atmospheric CO_2 inversions; in turn, the assimilation
280 of GOSAT and OCO-2 atmospheric CO_2 observations (54) should further constrain
281 CARDAMOM NCE estimates and their associated uncertainties. In this manner, non-
282 steady state C fluxes can ultimately be reconciled with ecosystem state and process
283 variables, such as C stocks and residence times.

The CARDAMOM approach provides a framework to test alternative model structures (55): in this manner, combined C cycle model parametric and structural uncertainties can be characterized, while ensuring consistency between models and global-scale datasets. This assessment would amount to a major step forward from conventional C cycle model inter-comparison studies. Ultimately an ensemble of models can be used to determine the degree to which retrievals of key C state and process variables are model-dependent. Moreover, alternative model structures could be used in CARDAMOM to assimilate globally spanning plant traits related to C cycling (56) and satellite observations such as solar-induced fluorescence (27), vegetation optical depth (57), soil moisture (58, 59) and changes in above-ground biomass (25, 60, 61). We anticipate that the incorporation of additional datasets and alternative model structures into CARDAMOM will generate quantifiable reductions in retrieved C variable uncertainties and new ecological insights on the state of terrestrial C cycle.

Materials and Methods

We grid MODIS LAI, ABGB (24), and HWSD topsoil and subsoil (0-100cm) C density (23) at a 1°×1° resolution (section S1 of the SI). The Data Assimilation Linked Ecosystem Carbon model version two (DALEC2) is analytically described by (35); an overview of DALEC2 C fluxes and pools is shown in Fig. 1. The 17 DALEC2 parameters (controlling the processes of photosynthesis and phenology, allocation, and turnover rates) and six

306 initial C pools robustly characterize terrestrial ecosystem C balance (19). DALEC2 is a
307 generic representation of C-cycling, where plant-functional types (PFTs) are not explicit:
308 instead, model parameters are treated as unknown and independent quantities for each
309 1°×1° grid cell (Table S1). We incorporate a fire C loss parameterization to account for
310 seasonal and inter-annual variations in fire C fluxes from DALEC2 (section S2 of the SI).
311 The model drivers consist of monthly time-step ERA interim meteorology and MODIS
312 burned area (34) at a 1°×1° resolution.
313
314 For each 1° x 1° grid cell, we use Bayesian inference to retrieve the probability of
315 DALEC2 model parameters $\mathbf{x}_i$ (Table S1) given observational constraints $\mathbf{O}_i$, henceforth
316 $\mathbf{p}(\mathbf{x}_i|\mathbf{O}_i)$, where
317
318 $$\mathbf{p}(\mathbf{x}_i|\mathbf{O}_i) \propto \mathbf{p}(\mathbf{x}_i)\,\mathbf{p}(\mathbf{O}_i|\mathbf{x}_i) \quad (1)$$
319
320 $\mathbf{p}(\mathbf{x}_i)$ is the prior parameter information and $\mathbf{p}(\mathbf{O}_i|\mathbf{x}_i)$ is the likelihood of $\mathbf{x}_i$ with respect to
321 $\mathbf{O}_i$. We use a Markov Chain Monte Carlo algorithm to sample $\mathbf{x}_i$ from $\mathbf{p}(\mathbf{x}_i|\mathbf{O}_i)$: we
322 henceforth refer to the retrieved DALEC2 parameter values at pixel *i* as $\mathbf{y}_i$. Within each
323 grid cell, C allocation fractions, residence times within each C pool, stocks, LCMA, and
324 associated C fluxes are derived from 4000 samples of $\mathbf{y}_i$ (section S3 of the SI). We hence
325 obtain a probability density function (PDF) for all C cycle variables within each 1°×1° grid
326 cell.
327

328 We do not impose PFT specific prior parameter distributions, or steady state
329 assumptions: $\mathbf{p}(\mathbf{x}_i)$ consists of ecologically viable parameter ranges (Table S1) and
330 ecological and dynamical constraints (35). Together these guarantee ecologically
331 consistent parameter retrievals within a globally prescribed parameter space, without
332 imposing spatially explicit prior parameter information.
333
334 From the C state and process variable estimates within each 1°×1° grid cell we use 4000
335 samples of $\mathbf{y}_i$ to determine the mean, median, mode, and %ile ranges for each C state
336 and process variable ranges. In Fig. 2-4, we present C allocation, residence time and C
337 stock 5th, 25th, median, 75th and 95th %iles at four selected locations: **B**: boreal [62.5°N,
338 81.5°E]; **T**: temperate [40.5°N, 120.5°W]; **D**: dry tropics [12.5°N, 20.5°E] and **W**: wet
339 tropics [7.5°S, 60.5°W]. We chose **B**, **T**, **D** and **W** as representative examples for C state
340 and process variable values within each area (the full 1°×1° C state and process variable
341 maps are shown in Fig. S1). To determine the robustness of our C state and process
342 variable estimates, we perform dedicated sensitivity tests to characterize the role of
343 systematic errors in data constraints and model structure: we repeat our C variable
344 retrievals using ±20% LAI, ±20% ABGB, ±20% HWSD, ±20% combustion coefficients,
345 alternative GPP (36) and limited heterotrophic respiration at <°0C (section S4 of the SI).
346
347 We compare our results against in-situ and regional observations of C allocation, pools
348 and residence times (section S5 of the SI), and we evaluate the resulting fluxes against
349 atmospheric CO_2 observations across 12 Total Carbon Column Observing Network sites

350 (38) by incorporating NCE results in a 4D atmospheric transport model (29). To
351 determine whether global land-cover types can predict the spatial variability of our
352 results, we conduct a multiple correlation coefficient analysis between C state and
353 process variables and 18 GLOBCOVER land-cover fractions at 1°×1°. We also employed a
354 principal component analysis on C state and process variables to retrieve the primary
355 1°×1° empirical orthogonal functions (EOFs). The details of the CARDAMOM results
356 evaluation and analyses are fully described in sections S5-8 of the SI. Statistical
357 abbreviations throughout the text include *r* (Pearson correlation coefficient), *RMSE*
358 (root-mean-square error). All spatially derived *r* and *RMSE* values reported in the text
359 are area-weighted. Retrieved C variable ranges – reported as area-weighted 25^{th} – 75^{th}
360 %iles – are derived from 1°×1° mean allocation and C stocks, log-based mean C
361 residence times (Fig. S1) and median LCMA values (Fig. 6). All CARDAMOM datasets
362 presented in this study can be downloaded from datashare.is.ed.ac.uk/
363 handle/10283/875.
364
365 **Acknowledgements**
366
367 AAB, JE, LF and MW were funded by the NERC National Centre for Earth Observation
368 (NCEO), UK. This work made use of the Edinburgh Compute and Data Facility resources
369 (ECDF, ecdf.ed.ac.uk). The research leading to these results has received funding from
370 the European Union's FP7 (2007-2013) under grant agreement no. 283080, project
371 GEOCARBON. IV was financially supported under a Netherlands Organization for

Scientific Research project (VIDI: 864.08.012). The TCCON Network is supported by NASA's Carbon Cycle Science Program through a grant to the California Institute of Technology. Part of this research was carried out at the Jet Propulsion Laboratory, California Institute of Technology, under a contract with the National Aeronautics and Space Administration.

Contributions

AAB and MW conceived the research. AAB undertook the research with assistance from JE, IV, MW and LF. AAB and MW wrote the paper with assistance from the other authors.

References

1. Le Quéré C, et al. (2013) The global carbon budget 1959–2011. *Earth System Sci Data* 5(1): 165-185.

2. Gatti LV, et al. (2014) Drought sensitivity of Amazonian carbon balance revealed by atmospheric measurements. *Nature* 506(7486): 76-80.

3. Dieleman WIJ, et al. (2012) Simple additive effects are rare: a quantitative review of plant biomass and soil process responses to combined manipulations of CO2 and temperature. *Global Change Biol* 18(9): 2681-2693.

4. Keenan TF, et al. (2013) Increase in forest water-use efficiency as atmospheric carbon dioxide concentrations rise. *Nature* 499(7458): 324-327.

396 5. Reich PB, Hobbie SE (2013) Decade-long soil nitrogen constraint on the CO2 fertilization of plant biomass. *Nature*
397 *Clim Change* 3(3): 278-282.
398
399 6. Schimel D, Stephens BB, Fisher JB (2015) Effect of increasing CO_2 on the terrestrial carbon cycle. *Proc Natl Acad Sci*
400 112(2): 436-441.
401
402 7. Cox PM, et al. (2013) Sensitivity of tropical carbon to climate change constrained by carbon dioxide variability.
403 *Nature* 494(7437): 341-344.
404
405 8. Todd-Brown KEO, et al. (2013) Causes of variation in soil carbon simulations from CMIP5 Earth system models and
406 comparison with observations. *Biogeosci* 10(3): 1717-1736.
407
408 9. Friend AD, et al. (2014) Carbon residence time dominates uncertainty in terrestrial vegetation responses to future
409 climate and atmospheric CO_2. *Proc Natl Acad Sci* 111(9): 3280-3285.
410
411 10. Atkin OK, et al. (2015) Global variability in leaf respiration in relation to climate, plant functional types and leaf
412 traits. *New Phytol* 206(2): 614-636.
413
414 11. Lewis SL, Brando PM, Phillips OL, van der Heijden GMF, Nepstad D (2011) The 2010 Amazon Drought. *Science*
415 331(6017): 554-554.
416
417 12. Luo, Y, Weng E (2011) Dynamic disequilibrium of the terrestrial carbon cycle under global change. *Trends in Ecol &*
418 *Evol* 26(2): 96-104.
419
420 13. Trumbore S (2006) Carbon respired by terrestrial ecosystems–recent progress and challenges. *Glob Change Biol*
421 12(2): 141-153.
422
423 14. Randerson JT, et al. (2005) Fire emissions from C3 and C4 vegetation and their influence on interannual variability
424 of atmospheric CO2 and δ13CO2. *Glob Biogeochem Cycles* 19(2)

15. Bloom AA, et al. (2015) Remote-sensing constraints on South America fire traits by Bayesian fusion of atmospheric and surface data. *Geophys Res Lett* 42(4): 1268-1274.

16. Bloom AA, Palmer PI, Fraser A, Reay DS (2012) Seasonal variability of tropical wetland CH_4 emissions: the role of the methanogen-available carbon pool. *Biogeosci* 9(8): 2821-2830.

17. Melton JR, et al. (2013) Present state of global wetland extent and wetland methane modelling: conclusions from a model intercomparison project (WETCHIMP). *Biogeosci* 10: 753-788.

18. Baldocchi D, et al. (2001) FLUXNET: A new tool to study the temporal and spatial variability of ecosystem-scale carbon dioxide, water vapor, and energy flux densities. *Bull Am Meteorol Soc* 82(11): 2415-2434.

19. Williams M, Schwarz PA, Law BE, Irvine J, Kurpius MR (2005) An improved analysis of forest carbon dynamics using data assimilation *Glob Change Biol* 11(1): 89-105.

20. Malhi Y, Saatchi S, Girardin C, Aragão LEOC (2009) The production, storage, and flow of carbon in Amazonian forests. *Amazonia and Glob Change* (2009): 355-372.

21. De Kauwe MG, et al. (2014) Where does the carbon go? A model–data intercomparison of vegetation carbon allocation and turnover processes at two temperate forest free-air CO2 enrichment sites. *New Phytol* 203(3): 883-899.

22. Huntzinger DN, et al. (2013) The north american carbon program multi-scale synthesis and terrestrial model intercomparison project–part 1: Overview and experimental design. *Geosci Model Development* 6(6): 2121-2133.

23. Hiederer R, Köchy M (2011) Global Soil Organic Carbon Estimates and the Harmonized World Soil Database. *EUR 25225 EN.* Publications Office of the European Union. 79pp.

24. Saatchi SS, et al. (2011) Benchmark map of forest carbon stocks in tropical regions across three continents. *Proc Natl Acad Sci* 108(24): 9899-9904.

25. Baccini AGSJ, et al. (2012) Estimated carbon dioxide emissions from tropical deforestation improved by carbon-density maps. *Nature Clim Change* 2(3):182-185.

26. Yokota T, et al. (2009) Global concentrations of CO_2 and CH_4 retrieved from GOSAT: First preliminary results. *Sola* 5: 160-163.

27. Frankenberg C, et al. (2011) New global observations of the terrestrial carbon cycle from GOSAT: Patterns of plant fluorescence with gross primary productivity. *Geophys Res Lett* 38(17).

28. Peters W, et al. (2010) Seven years of recent European net terrestrial carbon dioxide exchange constrained by atmospheric observations. *Glob Change Biol* 16(4): 1317-1337.

29. Feng L, et al. (2011) Evaluating a 3-D transport model of atmospheric CO_2 using ground-based, aircraft, and space-borne data. *Atmospheric Chem and Phys* 11(6): 2789-2803.

30. Beer C, et al. (2010) Terrestrial gross carbon dioxide uptake: global distribution and covariation with climate. *Science* 329(5993): 834-838.

31. Carvalhais N, et al. (2014) Global covariation of carbon turnover times with climate in terrestrial ecosystems. *Nature* 514: 213–217.

32. Mahecha MD, et al. (2010) Global convergence in the temperature sensitivity of respiration at ecosystem level. *Science* 329(5993): 838-840.

33. Ziehn T, Scholze M, Knorr W (2012) On the capability of Monte Carlo and adjoint inversion techniques to derive posterior parameter uncertainties in terrestrial ecosystem models. *Glob Biogeochem Cycles* 26(3).

34. Giglio L, Randerson JT, van der Werf GR (2013) Analysis of daily, monthly, and annual burned area using the fourth-generation global fire emissions database (GFED4). *J Geophys Res*: *Biogeosci* 118(1): 317-328.

35. Bloom AA, Williams M. (2015) Constraining ecosystem carbon dynamics in a data-limited world: integrating ecological" common sense" in a model–data fusion framework. *Biogeosci* 12(5): 1299-1315.

36. Jung M, Reichstein M, Bondeau A (2009) Towards global empirical upscaling of FLUXNET eddy covariance observations: validation of a model tree ensemble approach using a biosphere model. *Biogeosci* (6)10: 2001-2013.

37. van der Werf GR, et al. (2010) Global fire emissions and the contribution of deforestation, savanna, forest, agricultural, and peat fires (1997–2009). *Atmospheric Chem and Phys* 10(23): 11707-11735.

38. Wunch D, et al. (2011) The total carbon column observing network. *Phil Trans Roy Soc A,* 369(1943): 2087-2112.

39. Malhi Y, et al. (2015) The linkages between photosynthesis, productivity, growth and biomass in lowland Amazonian forests. *Glob Change Biol* 21(6): 2283-2295.

40. Thurner M. et al. (2014) Carbon stock and density of northern boreal and temperate forests. *Global Ecology and Biogeography* 23(3): 297-310.

41. Bontemps, S., et al. (2011) GLOBCOVER 2009-Products description and validation report.

42. Lehmann CER, et al. (2014) Savanna vegetation-fire-climate relationships differ among continents. *Science* 343(6170): 548-552.

43. Reich PB, et al. (2014) Biogeographic variation in evergreen conifer needle longevity and impacts on boreal forest carbon cycle projections. *Proc Natl Acad Sci* 111(38): 13703-13708.

511 44. Sterck F, et al. (2011) Functional traits determine trade-offs and niches in a tropical forest community. *Proc Natl*
512 *Acad Sci* 108(51): 20627-20632.
513
514 45. Wright IJ, et al. (2004) The worldwide leaf economics spectrum. *Nature* 428(6985): 821-827.
515
516 46. Todd-Brown KE, et al. (2013) Causes of variation in soil carbon simulations from CMIP5 Earth system models and
517 comparison with observations. *Biogeosci* 10(3): 1717-1736
518
519 47 Trumbore, S (2000) Age of soil organic matter and soil respiration: radiocarbon constraints on belowground C
520 dynamics. *Ecol Appl* 10(2): 399-411.
521
522 48: Doetterl S, Six J, van Wesemael B, van Oost K (2012) Carbon cycling in eroding landscapes: geomorphic controls on
523 soil organic C pool composition and C stabilization. *Glob Change Biol* 18(7): 2218-2232.
524
525 49: Wild B, et al. (2014) Input of easily available organic C and N stimulates microbial decomposition of soil organic
526 matter in arctic permafrost soil. *Soil Biol Biochem*, 75: 143-151.
527
528 50. Exbrayat J, Williams M (2015) Quantifying the net contribution of the historical Amazonian deforestation to
529 climate change. *Geophys Res Lett* 42.8: 2968-2976.
530
531 51. Amiro BD, Stocks BJ, Alexander ME, Flannigan MD, Wotton BM (2001) Fire, climate change, carbon and fuel
532 management in the Canadian boreal forest. *Internat J of Wildland Fire* 10(4): 405-413.
533
534 52. Heiskanen J, et al (2012) Seasonal variation in MODIS LAI for a boreal forest area in Finland. *Remote Sens of*
535 *Environ*, 126: 104-115.
536
537 53. Schimel D, et al. (2015) Observing terrestrial ecosystems and the carbon cycle from space. *Glob change biol*, 21(5):
538 1762-1776.
539

54. Crisp D, Miller CE, DeCola PL (2008) NASA Orbiting Carbon Observatory: measuring the column averaged carbon dioxide mole fraction from space. *J Applied Remote Sens* 2(1): 23508.

55. Keenan TF, Carbone MS, Reichstein M, Richardson A (2011) The model–data fusion pitfall: assuming certainty in an uncertain world. *Oecologia* 167(3): 587-597.

56. Kattge J, et al. (2011) TRY–a global database of plant traits. *Glob Change Biol* 17(9): 2905-2935.

57. Lawrence H, et al. (2014) Comparison between SMOS Vegetation Optical Depth products and MODIS vegetation indices over crop zones of the USA. *Remote Sens of Environ* 140: 396-406.

58. Kerr YH, et al. (2010) The SMOS mission: New tool for monitoring key elements of the global water cycle. *Proc of the IEEE* 98,(5): 666-687.

59. Entekhabi D, et al. (2010) The soil moisture active passive (SMAP) mission. *Proc of the IEEE* 98(5): 704-716.

60. Le Toan T, et al. (2011) The BIOMASS mission: Mapping global forest biomass to better understand the terrestrial carbon cycle. *Remote Sens of Environ* 115(11): 2850-2860.

61. Liu YY, et al. (2015) Recent reversal in loss of global terrestrial biomass. *Nature Clim Change* 5:470-474.

62. DeLucia EH, Drake JE, Thomas RB, Gonzales-Meler M (2007) Forest carbon use efficiency: is respiration a constant fraction of gross primary production? *Glob Change Biol* 13(6): 1157-1167.

63. Feng L, et al. (2015) Elevated uptake of CO_2 over Europe inferred from GOSAT XCO_2 retrievals: a real phenomenon or an artefact of the analysis? *Atmos Chem and Phys Discus* 15(2): 1989-2011.

64. Huntzinger DN, et al. (2015, in press). NACP MsTMIP: Global 0.5-deg Terrestrial Biosphere Model Outputs (version 1) in Standard Format. Dataset available on-line [http://daac.ornl.gov]. DOI: 10.3334/ORNLDAAC/1225

569

570 65. Metcalfe DB, et al. (2008) The effects of water availability on root growth and morphology in an Amazon
571 rainforest. *Plant and Soil* 311(1-2) 189-199.

572

573 66. Burke MK, Raynal DJ (1994) Fine root growth phenology, production, and turnover in a northern hardwood forest
574 ecosystem. *Plant and soil* 162(1): 135-146.

575

576 67. Gill RA, Jackson RB (2000) Global patterns of root turnover for terrestrial ecosystems. *New Phytol* 147(1): 13-31.

577

578 68. Sloan VL, Fletcher BJ, Press MC, Williams M, Phoenix GK (2013) Leaf and fine root carbon stocks and turnover are
579 coupled across Arctic ecosystems. *Glob Change Biol* 19(12): 3668-3676.

580

581 **Figure captions**

582

583 **Fig. 1:** Diagnostic ecosystem carbon (C) balance model DALEC2 (19,35) and datasets
584 used to retrieve 1°×1° C state and process variables. Gross primary production (GPP), a
585 function of climate and foliar C, is partitioned into autotrophic respiration (Ra) and net
586 primary production (NPP). NPP is partitioned into the live biomass pools. Plant mortality
587 provides input to the dead organic matter (DOM) pools. Heterotrophic respiration (Rh)
588 is derived from decomposing DOM pools. Fire fluxes are derived from burned area data
589 (35) and all C pools (see section S3). Within each 1° x 1° grid cell, we use a Bayesian
590 model-data fusion algorithm to retrieve C state/process variables and uncertainties;
591 variables are retrieved without prior land-cover type or steady state assumptions. Data
592 constraints consist of MODIS leaf area, total biomass (24, tropics only) and soil C (23).

593 Details on the Bayesian fusion approach are provided in the Materials and Methods
594 section.
595
596 **Fig. 2:** Retrievals of net primary production (NPP) allocation to structural (wood and fine
597 roots) and photosynthetic (labile and foliage) C pools. Allocation fractions were
598 retrieved at 1°×1° using a Bayesian model-data fusion approach (Fig. 1). The gross
599 primary production allocation fraction retrievals at locations B, T, D and W are shown in
600 the three right-hand panels (median = black dot, 50% confidence range = box and 90%
601 confidence range = line).
602
603 **Fig. 3:** Retrievals of C residence time (RT) in live biomass and dead organic matter C
604 pools; residence times are retrieved at 1° x 1° using a Bayesian model-data fusion
605 approach (Fig. 1). Brown colors denote ecosystems with high residence times for all C
606 pools, green areas denote ecosystems with long live biomass C residence times and
607 orange areas denote ecosystems with low live biomass residence time. The residence
608 times for individual C pools at locations B, T, D and W are shown in the three right-hand
609 panels (median = black dot, 50% confidence range = box and 90% confidence range =
610 line). Mean C residence times by (31) are shown as grey boxes (50% confidence interval)
611 and black dots (median).
612
613 **Fig.4:** Retrieved mean photosynthetic (foliar and labile) and structural (wood and fine
614 roots) C pool stocks; C stocks are retrieved at 1° x 1° using a Bayesian model-data fusion

615 approach (Fig. 1). Retrieved mean C stocks for each pool at locations B, T, D and W are
616 shown in the four right-hand panels (median = black dot, 50% confidence range = box
617 and 90% confidence range = line). Dark colors denote high structural C/high
618 photosynthetic C ecosystems, green colors denote low structural C/high photosynthetic
619 C ecosystems, red colors denote low photosynthetic C/high structural C ecosystems, and
620 yellow colors denote low photosynthetic C/low structural C ecosystems.
621
622 **Fig. 5. Top:** Retrieved median 1° x 1° leaf C mass per leaf area (LCMA, gC m^{-2}). **Top right:**
623 zonal mean of median LCMA and 50% confidence range. **Bottom:** LCMA against leaf
624 lifespan for high latitudes (>55°N/S), temperate regions (23°–55°N/S), dry tropics
625 (precip.<1500mm, <23°N/S) and wet tropics (precip.>1500mm, <23°N/S).
626
627 **Fig. 6.** Multiple correlation coefficients (R, x-axis) of retrieved C state and process
628 variables (allocation fractions, residence times, mean C pools and LCMA; y-axis) against
629 18 GLOBCOVER land-cover fractions and C variable primary empirical orthogonal
630 functions (EOFs). R denotes the ability of GLOBCOVER land-cover types and primary
631 EOFs to predict 1° x 1° state and process variables (R would equal 1 if all C state and
632 process variables could be expressed as a linear sum of land-cover fractions or EOFs).

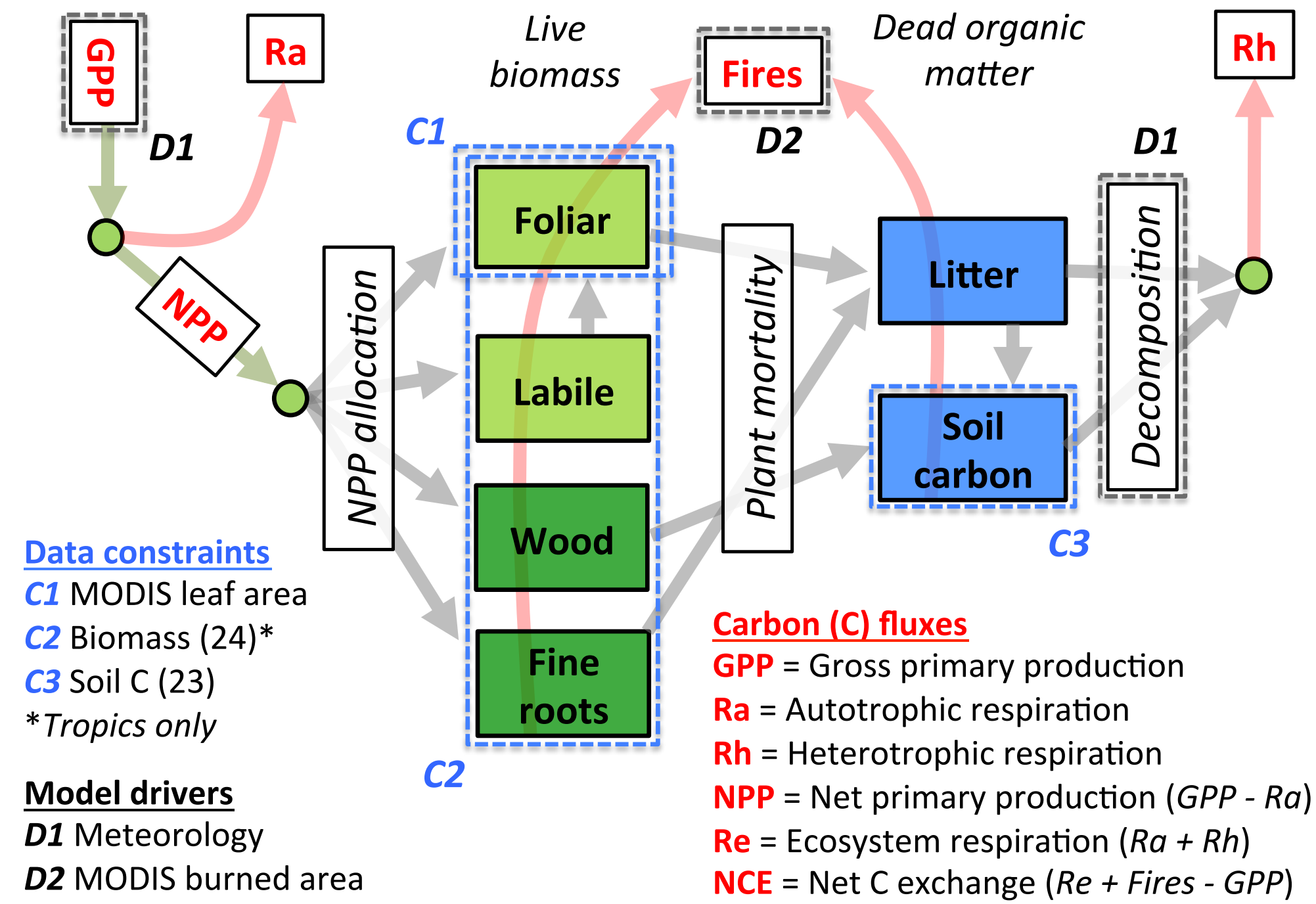

Data constraints

C1 MODIS leaf area

C2 Biomass (24)*

C3 Soil C (23)

**Tropics only*

Model drivers

D1 Meteorology

D2 MODIS burned area

Carbon (C) fluxes

GPP = Gross primary production

Ra = Autotrophic respiration

Rh = Heterotrophic respiration

NPP = Net primary production (*GPP - Ra*)

Re = Ecosystem respiration (*Ra + Rh*)

NCE = Net C exchange (*Re + Fires - GPP*)

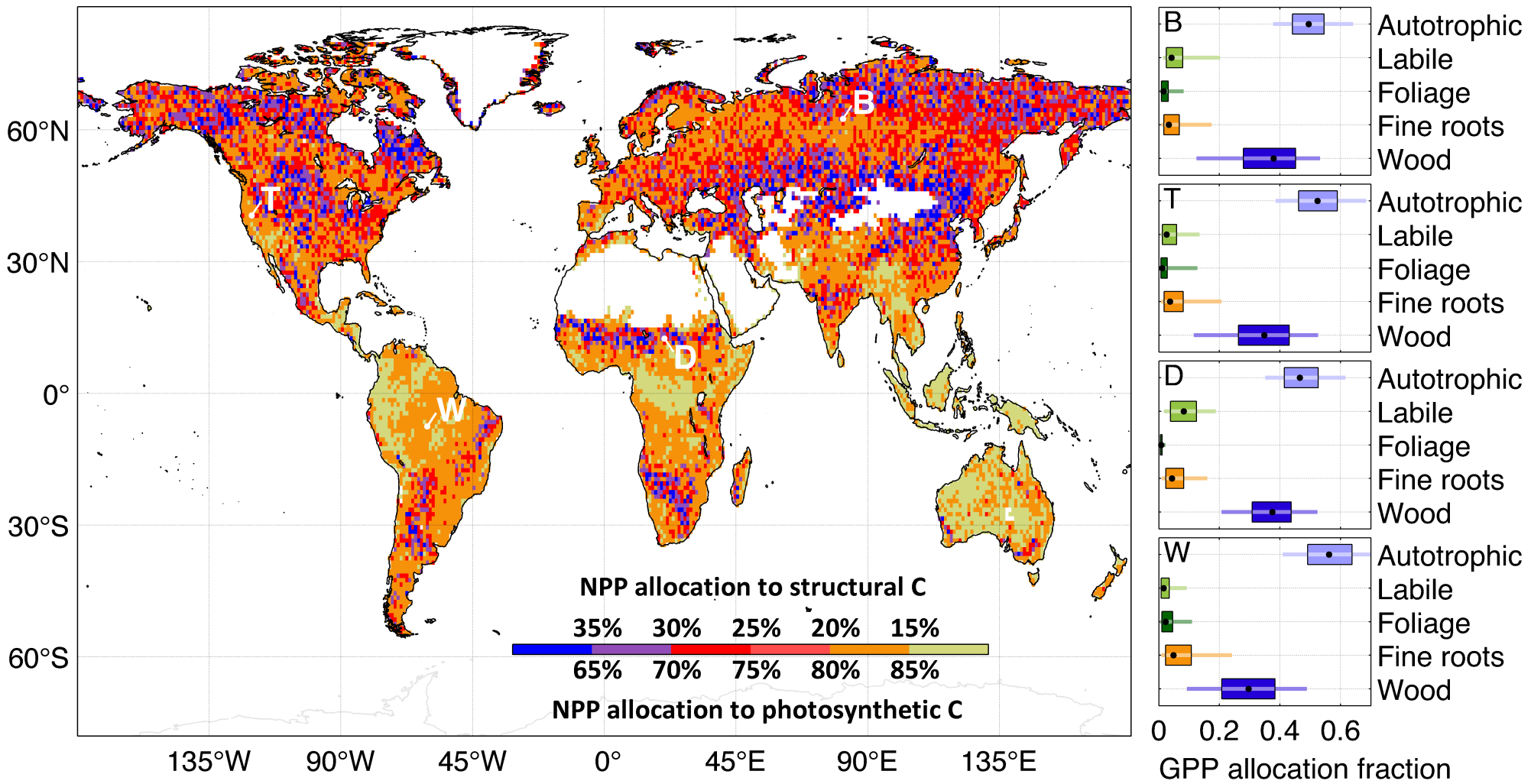
B
T
D
W
60°N
30°N
0°
30°S
60°S
135°W
90°W
45°W
0°
45°E
90°E
135°E
NPP allocation to structural C
35% 30% 25% 20% 15%
65% 70% 75% 80% 85%
NPP allocation to photosynthetic C
B
Autotrophic
Labile
Foliage
Fine roots
Wood
T
Autotrophic
Labile
Foliage
Fine roots
Wood
D
Autotrophic
Labile
Foliage
Fine roots
Wood
W
Autotrophic
Labile
Foliage
Fine roots
Wood
0 0.2 0.4 0.6
GPP allocation fraction

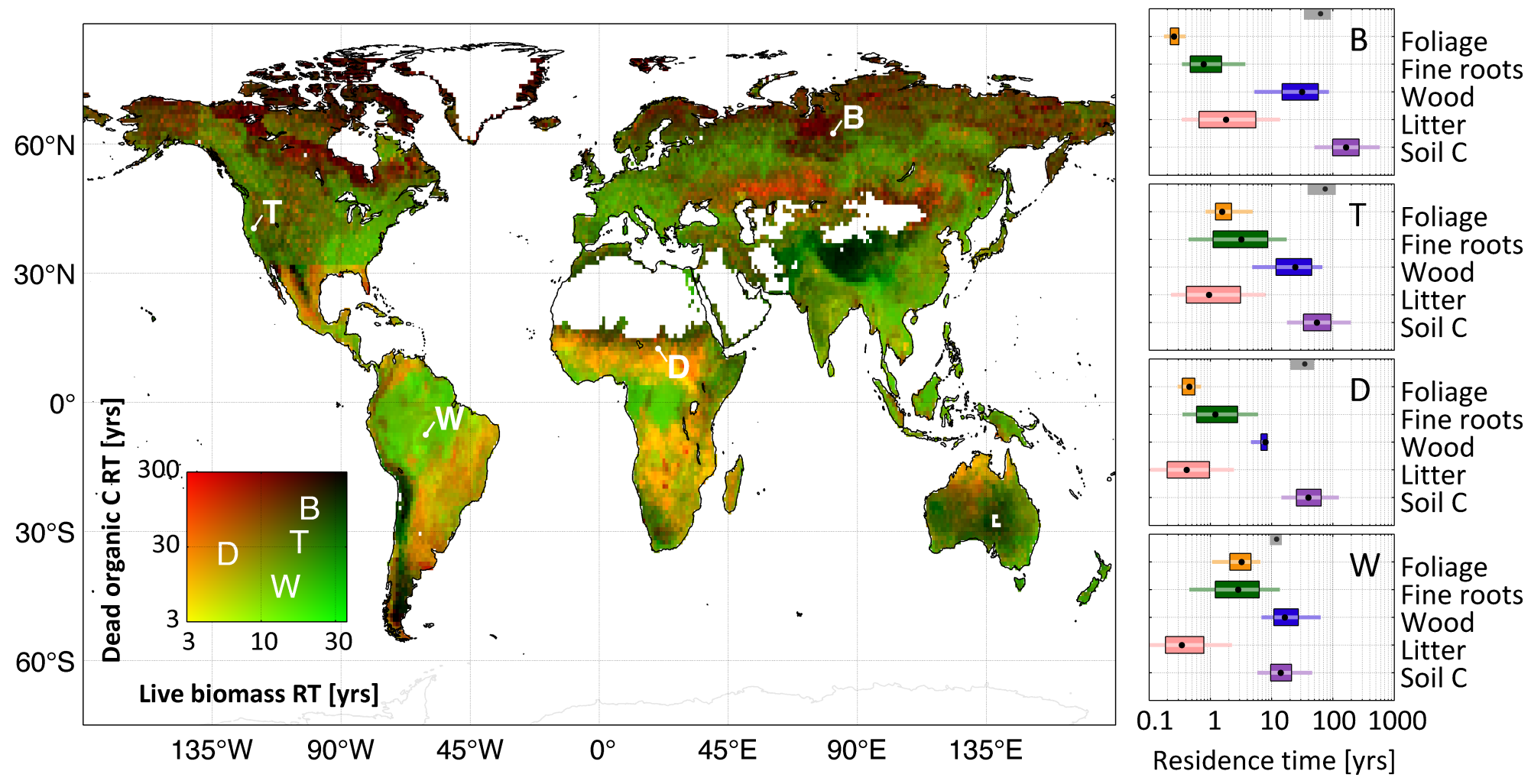
60°N
30°N
0°
30°S
60°S
135°W
90°W
45°W
0°
45°E
90°E
135°E
B
T
D
W
Dead organic C RT [yrs]
300
30
3
3
10
30
Live biomass RT [yrs]
Foliage
Fine roots
Wood
Litter
Soil C
0.1
1
10
100
1000
Residence time [yrs]

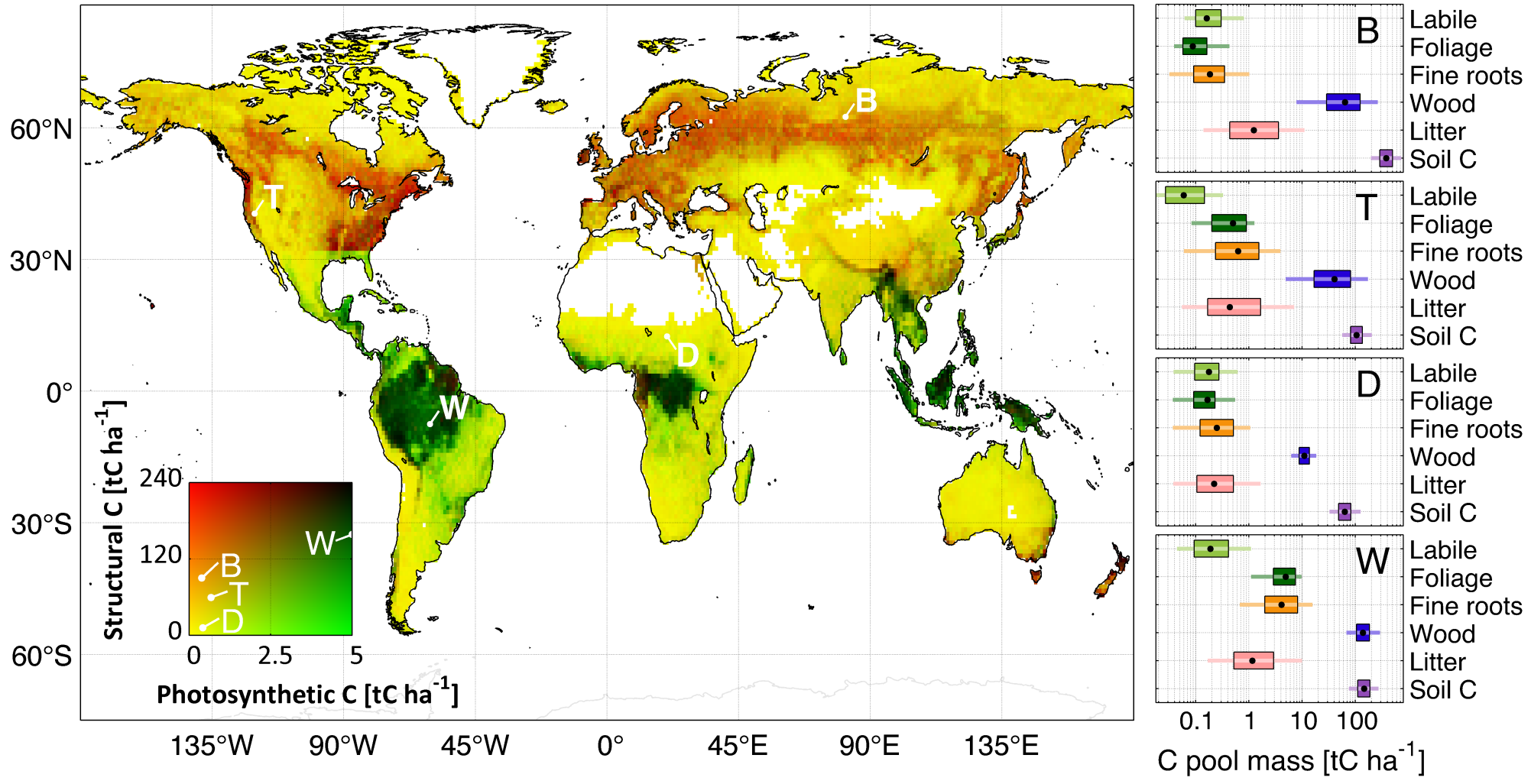
60°N
30°N
0°
30°S
60°S
135°W
90°W
45°W
0°
45°E
90°E
135°E
B
T
D
W
Structural C [tC ha-1]
240
120
0
0
2.5
5
Photosynthetic C [tC ha-1]
B
Labile
Foliage
Fine roots
Wood
Litter
Soil C
T
Labile
Foliage
Fine roots
Wood
Litter
Soil C
D
Labile
Foliage
Fine roots
Wood
Litter
Soil C
W
Labile
Foliage
Fine roots
Wood
Litter
Soil C
0.1
1
10
100
C pool mass [tC ha-1]

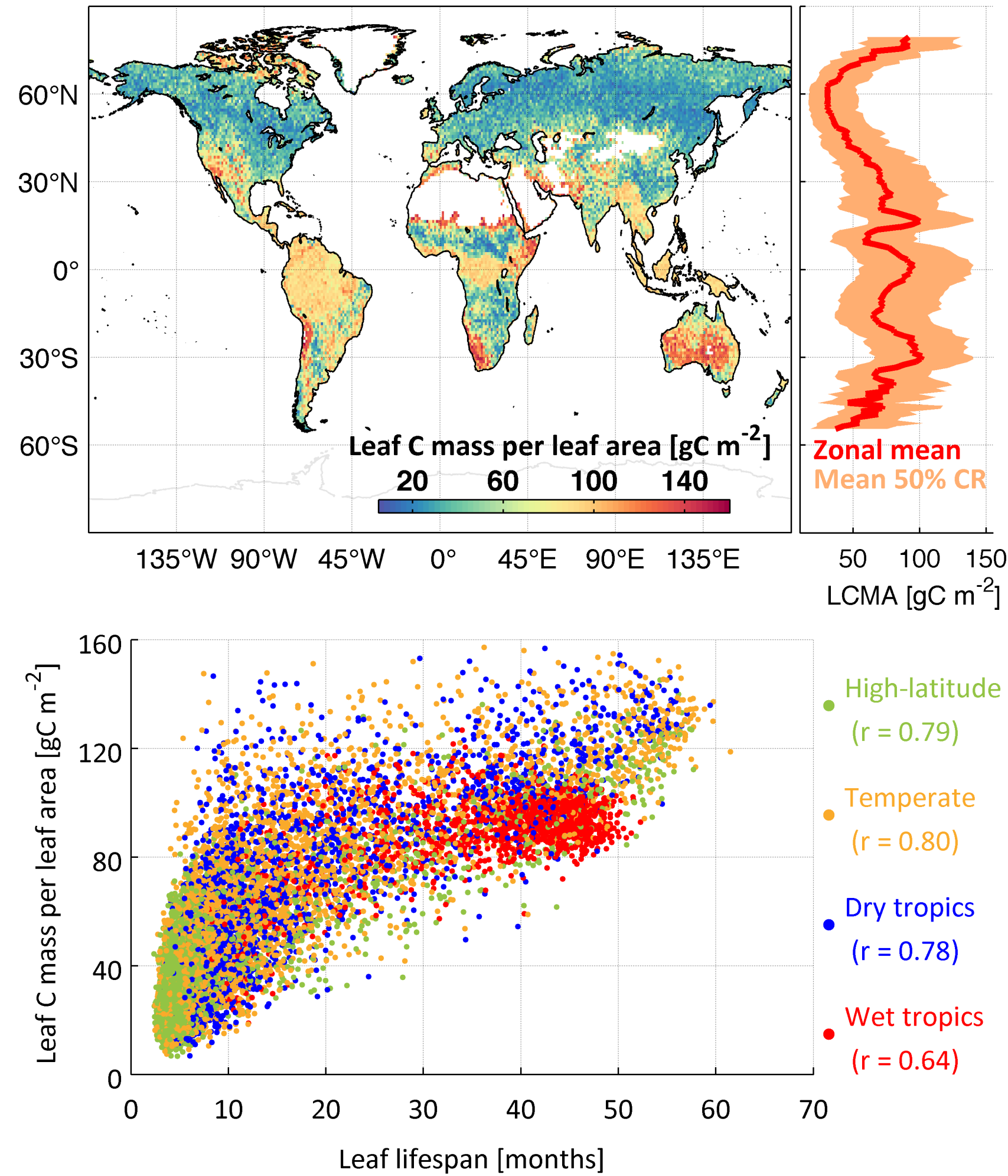
60°N
30°N
0°
30°S
60°S
135°W 90°W 45°W 0° 45°E 90°E 135°E
Leaf C mass per leaf area [gC m-2]
20 60 100 140
Zonal mean
Mean 50% CR
50 100 150
LCMA [gC m-2]
Leaf C mass per leaf area [gC m-2]
160
120
80
40
0
0 10 20 30 40 50 60 70
Leaf lifespan [months]
High-latitude
(r = 0.79)
Temperate
(r = 0.80)
Dry tropics
(r = 0.78)
Wet tropics
(r = 0.64)

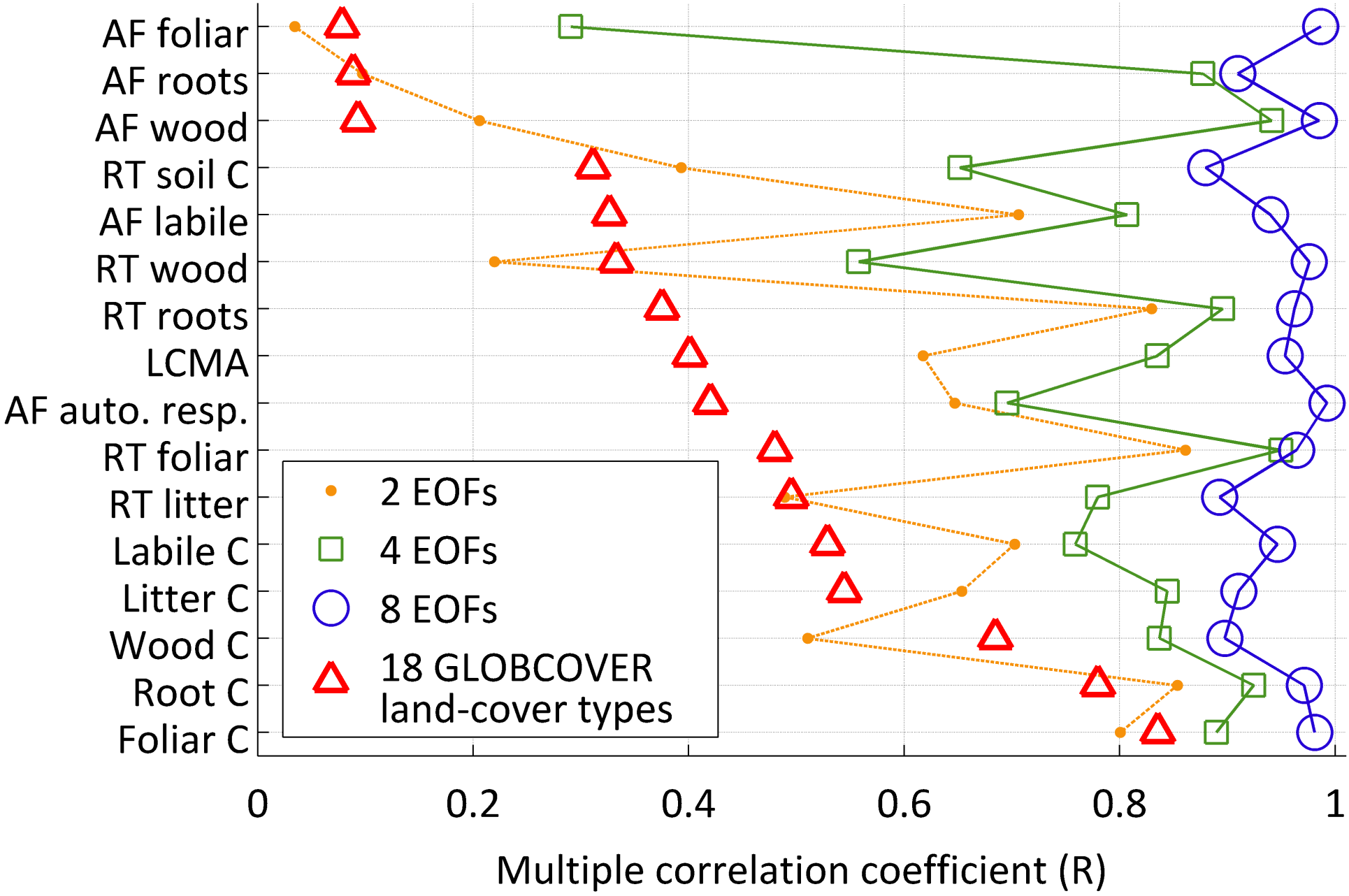
AF foliar
AF roots
AF wood
RT soil C
AF labile
RT wood
RT roots
LCMA
AF auto. resp.
RT foliar
RT litter
Labile C
Litter C
Wood C
Root C
Foliar C
2 EOFs
4 EOFs
8 EOFs
18 GLOBCOVER land-cover types
0
0.2
0.4
0.6
0.8
1
Multiple correlation coefficient (R)

Supporting information

"The decadal state of the terrestrial carbon cycle: global retrievals of terrestrial carbon allocation, pools and residence times".

A. Anthony Bloom[1,2,3], Jean-François Exbrayat[2,3], Ivar van der Velde[4], Liang Feng[2,3], Mathew Williams[2,3]

1. Jet Propulsion Laboratory, California Institute of Technology, Pasadena, CA, USA
2. School of GeoSciences, University of Edinburgh, Edinburgh, UK
3. National Centre for Earth Observation, Edinburgh, UK
4. Wageningen University, Wageningen, The Netherlands

S1. Global 1° × 1° grid model-data fusion

Global datasets. We grid the 30-second Harmonized World Soil Database soil carbon (C) density (HWSD, based on national inventories of top 1 m soil bulk density and organic C content) (23) and a ~1km × 1km above- and below-ground pan-tropical biomass map (24) at 1° × 1°. We grid the MOD15A2 MODIS LAI product (1km **×** 1km) and a MODIS Burned Area product (0.25° × 0.25°) (34) at a 1° × 1° monthly resolution for each month within the period 2001-2010. While finer spatial/temporal resolutions can potentially be implemented, we chose a 1° × 1° monthly resolution as a consequence of the computational cost of our approach. We use ERA-interim 1° × 1° monthly re-analysis products as DALEC2 drivers; see (35) for MODIS quality flag and ERA-interim driver details. We exclude 1° × 1° grid-cells where desert and ice-covered areas account for more than 90% of the grid-cell land-cover (based on GLOBCOVER 2009 Global land-cover maps, 41), as their role in the terrestrial C cycle is negligible.

Model-data fusion. Within each 1° × 1° degree grid cell *i*, we use the 1° × 1° aggregated biomass (tropics only), soil C and MODIS LAI datasets (observations $\mathbf{O}_i$) to constrain DALEC2 parameters $\mathbf{x}_i$ (for a complete description of the DALEC2 model and C pools, we refer the reader to (35) and references therein). We implement a Metropolis-Hastings Markov Chain Monte Carlo (MHMCMC, 33, 35) to determine the probability of $\mathbf{x}_i$ given observational constraints $\mathbf{O}_i$ (see equation 1 in main text).

The prior ranges of DALEC2 parameters $\mathbf{x}_i$ are shown in Table S1. We also imposed a prior log-normal distribution on autotrophic respiration fraction $x_{i,a}$ (autotrophic respiration = $0.5 \times 1.2^{\pm 1}$) and a prior log-normal distribution on canopy efficiency $x_{i,c}$ (canopy efficiency parameter = $17.5 \times 1.2^{\pm 1}$), where ±1 represents a normal distribution with mean 0 and variance 1. These constraints yield a range of results that are broadly consistent with the global GPP range reported by (30) and represent the range of autotrophic respiration estimates reported by (62). The prior parameter probability, $\mathbf{p}(\mathbf{x}_i)$ is therefore expressed as:

$$\mathbf{p}(\mathbf{x}_i) = \mathbf{p}_{BW}(\mathbf{x}_i)\, e^{-0.5\left(\frac{log(x_{i,a})-log(0.5)}{log(1.2)}\right)^2} e^{-0.5\left(\frac{log(x_{i,c})-log(17.5)}{log(1.2)}\right)^2}, \quad (1)$$

where $\mathbf{p}_{BW}(\mathbf{x}_i)$ is the prior parameter probability described by (35). Within each 1° × 1° grid cell, we prescribe an uncertainty factor of 1.5 to mean 2001-10 HWSD soil C and total above and below-ground biomass density (i.e. mean labile + foliar + fine roots + wood), and an uncertainty factor of 2 to mean monthly MODIS LAI observations. For total biomass, given that the maximum entropy algorithm employed by (24) was based on bins of 12.5 tC ha^{-1}, we anticipate that low biomass density values (such as the edges of the Sahel and Kalahari deserts) exhibit comparable uncertainty. We therefore prescribe an uncertainty factor of *max(*1.5*,* 12.5*/B_i)*, where B_i is the total biomass density and the *max()* function denotes the maximum of the two values. The likelihood function $\mathbf{p}(\mathbf{O}_i|\mathbf{x}_i)$ is therefore expressed as:

$$\mathbf{p}(\mathbf{O}_i|\mathbf{x}_i) = \exp\left(-0.5\ \Sigma_{j=1}^{N}\left(\frac{M_{ij} - O_{ij}}{U_{ij}}\right)^2\right), \qquad (2)$$

where O_{ij} and U_{ij} are the j^{th} observations and uncertainty factors at location *i*, and M_{ij} is the equivalent DALEC2 model output based on parameter vector $\mathbf{x}_i$ (we note that O_{ij}, U_{ij} and M_{ij} are log-transformed, e.g. for a soil C value of 100 tC ha^{-1}, O_{ij} = log(100) and U_{ij} = log(1.5)). For each LAI observation, M_{ij} is the DALEC2 foliar C (on the corresponding month) divided by leaf C mass per leaf area. For biomass and soil C, M_{ij} is the DALEC2 soil C stock and mean live biomass (labile + foliar + fine roots + wood) on Jan 1st 2001. For the analytical description of DALEC2, the MHMCMC algorithm and $\mathbf{p}_{BW}(\mathbf{x}_i)$, we refer the reader to (35) and references therein; the DALEC2 fire module is described in section S3.

Ecological and Dynamical Constraints. The twelve Ecological and Dynamical Constraints (EDCs 1-12, 35) are a component of the prior parameter probability – $\mathbf{p}_{BW}(\mathbf{x}_i)$ – and consist of relative constraints on allocation parameters, turnover rates, growth rates, exponential decays and steady state proximity. When steady state is not assumed, steady state proximity conditions are necessary to distinguish between real and nonsensical C pool trajectories (35). We developed a simpler numeric equivalent of the steady state proximity EDCs (EDCs 9-12), to account for the stochastic C losses from fires. For each pool, we derive the steady state proximity factor (S_{prox}) as follows:

$$S_{prox} = \frac{\overline{\boldsymbol{C}_{input}}}{\overline{\boldsymbol{C}_{output}}}, \qquad (3)$$

where $\overline{\boldsymbol{C}_{input}}$ and $\overline{\boldsymbol{C}_{output}}$ are the mean inputs and outputs from each pool. We impose a steady state proximity condition of 0.5> S_{prox} >2 for each pool.

We found that EDC 8 – the ecological and dynamic constraint limiting rapid exponential pool trajectories – was excessively rigid for relatively small amounts of exponential pool trajectories (which can occur naturally and/or as a model artifact). Here we use a simpler approach to minimize the rapid exponential decay of C pools: we ensure that the steady state proximity of each C pool at time zero – $S_{prox(jan2001)}$ – is within 0.05 of S_{prox}, i.e.

$$\left|S_{prox} - S_{prox(jan2001)}\right| < 0.05. \qquad (4)$$

$S_{prox(jan2001)}$ can be derived as:

$$S_{prox(jan2001)} = S_{prox} \times \frac{\overline{C_{jan2001-10}}}{C_{jan2001}}, \quad (5)$$

where $\overline{C_{jan2001-10}}$ is the mean January C pool stock and $C_{(Jan2001)}$ is the C pool stock in January 2001. The CARDAMOM code used in this manuscript (DALEC2 model, EDCs and adaptive Metropolis-Hastings Markov Chain Monte Carlo) is available upon request.

S2. DALEC2 fire module

To determine the monthly C losses from fires at time *t*, we determine the monthly fraction of each grid cell burned, $B_{area(t)}$, based on the MODIS-derived burned area product (34). At each monthly time step, the fire losses within each 1° × 1° grid cell are derived as follows:

$$F_{e(t)} = B_{area(t)} \times \sum_{p=1}^{6} k_{factor(p)}\, C_{(p,t)}\ , \quad (6)$$

where $F_{e(t)}$ are the total fire C emissions at time *t,* $k_{factor(p)}$ is the combustion factor for pool *p,* and $C_{(p,t)}$ is the C in pool *p* at time *t*. We also impose a resilience factor *r* to the remaining pools within the burned area: from live biomass pool, a fire-mortality flux is derived from the un-combusted C pools as follows:

$$F_{m(t,p)} = B_{area(t)} \times (1 - k_{factor(p)})\,(1 - r) C_{(p,t)}, \quad (7)$$

The fire-mortality C flux from foliage, roots and labile is deposited into the litter pool, and fire mortality C flux from wood is transferred to the soil C pool. Equally, (1 - *r*) of un-combusted litter C is transferred to the soil C pool. The k_{factor} values for labile (0.1), foliar (0.9), root (0.1), wood (0.1), litter (0.5) and soil C (0.01) are broadly equivalent to the k_{factor} values used by the Global Fire Emission Database (37). We apply a resilience factor of r = 0.5. The sensitivity calculations associated with $k_{factor(p)}$ and r_f are described in section S4.

S3. Global state and process variables

The spatial distributions of individual C pool allocation fractions, residence times and stocks are shown in Fig. S1. The residence time for each C pool at grid cell *i* is derived as follows:

$$RT_{pool(j)} = \frac{C_{pool(j)}}{F_{in(j)} - \Delta C_{pool(j)}} \times 365.25, \quad (8)$$

where $C_{pool(j)}$ is the mean pool size, $F_{in(j)}$ is the mean daily C pool input and $\Delta C_{pool(j)}$ is the mean daily change in pool size throughout 2001-10 for the j^{th} parameter vector sample of $\mathbf{y}_i$ (i.e. $C_{pool(j)}$, $F_{in(j)}$ and $\Delta C_{pool(j)}$ are calculated from DALEC2 output driven with j^{th} parameter vector sample of $\mathbf{y}_i$). Mean live biomass (dead organic matter) pool residence times are derived based on equation 8, where $C_{pool(j)}$, $F_{in(j)}$ and $\Delta C_{pool(j)}$ are the total live biomass (dead organic matter) C corresponding to j^{th} parameter vector sample of $\mathbf{y}_i$. Leaf lifespan is equivalent to RT_{foliar}. Reported global and zonal 25^{th} – 75^{th} %ile ranges of total annual fluxes were derived from the sum of monthly 1° × 1° 25^{th} and 75^{th} %iles for each flux multiplied by the 1° × 1° grid cell area; the same approach was used to derive median fluxes and mode net C exchange (NCE).

Monthly mode NCE within each 1° × 1° grid-cell was derived by binning NCE samples into 0.01 gC m^{-2} day^{-1} intervals.

S4. Sensitivity Tests

We determine the sensitivity of C allocation, residence times and C pool size estimates at locations B, T, D and W (see Materials and Methods in main text for B, T, D and W coordinates) to LAI, biomass and soil C data constraints (sensitivity tests S1-S6), fire combustion and resilience factor coefficients (sensitivity test S7-S10), the use of MPI GPP (36) instead of the default DALEC (19) GPP (sensitivity test S11), and the suppression of heterotrophic respiration under -10°C (sensitivity test S12). The sensitivity experiments are summarized in Table S2. The results of the sensitivity tests are shown in Fig. S2.

S5 Comparison against in-situ and regional observations

CARDAMOM results are compared against a range of in-situ measurements in Table S3. We compare each in-situ measurement against the 50% and 90% confidence range of the mean 1° × 1° values within the stated region. Comparison details and footnotes are included in Table S3. We also compare CARDAMOM total biomass against a boreal forest biomass dataset derived from synthetic aperture radar data (BIOMASAR map, 40) aggregated to 1° × 1°. The CARDAMOM-to-BIOMASAR comparison is conducted for the total biomass across all 1° × 1° areas with at least 95% BIOMASAR map coverage; total BIOMASAR biomass within those areas is 38% lower than CARDAMOM biomass. We note that lower-than-expected LCMA estimates in boreal ecosystems (Fig. 6) could be explained by (i) understory plant traits (linked to deciduous shrubs); or (ii) seasonal MODIS LAI biases (53). In particular, the significant correlation between LCMA and leaf lifespan suggests that retrieved LCMA accuracy could be strongly linked to seasonal biases in MODIS LAI.

S6 Comparison to GLOBCOVER land-cover types and EOFs

For each 1° × 1° grid cell *i* we determine the fraction of each GLOBCOVER (41) land-cover type *L*, $F_{L(i)}$. We then determine the Pearson's correlation coefficients (r_{LS}) between $\mathbf{f}_L$ (the vector of all 1° × 1° land-cover type *L* fractions) and each C state and process variable vector $\mathbf{c}_S$ *(*the vector of each 1° × 1° state and process variable): state or process variables (denoted by subscript *S*) consist of allocation fractions, C residence times, C pool sizes and leaf C mass per leaf area. The r_{LS}^2 values between each GLOBCOVER land-cover type fraction *L* and each C state/process variable *S* are shown in Fig. S3. The land-cover categories are: irrigated croplands (**CRI**); Rainfed croplands (**CRR**); Mosaic cropland > vegetation (**MCV**); Mosaic vegetation > cropland (**MVC**); Closed to open broadleaved evergreen or semi-deciduous forest (**BESDF**); Closed broadleaved deciduous forest (**BDF**); Open broadleaved deciduous forest/woodland (**BDFW**); Closed (>40%) needleleaved evergreen forest (**NEF**); Open needleleaved deciduous or evergreen forest (**NDEF**); Closed to open mixed forest (**MF**); Mosaic forest or shrubland > grassland (**MFSG**); Mosaic grassland > forest or shrubland (**MGFS**); Closed to open shrubland (**SRB**); Closed to open herbaceous vegetation (**GRA**); Sparse vegetation (**SPA**); Closed to open broadleaved forest regularly flooded (**FWE**); forest or shrubland, permanently flooded (**SWE**); Closed to open vegetation on flooded or waterlogged soil (**WET**) (54).

The multiple correlation coefficient R_S between C state/process variable S and 18 GLOBCOVER land-cover type fractions is derived as follows:

$$R_S = \mathbf{r}_S^{\mathrm{T}} \, \mathbf{R}_{\mathrm{LL}}^{-1} \, \mathbf{r}_S, \quad (9)$$

where $\mathbf{r}_S$ is the 1 x 18 vector of correlations coefficients between state/process variable vector $\mathbf{c}_S$ and 18 1° × 1° land-cover type fraction vectors $\mathbf{f}_L$, $\mathbf{r}_s^{\mathrm{T}}$ is the transpose of $\mathbf{r}_s$, and $\mathbf{R}_{\mathrm{LL}}^{-1}$ is the inverse of the correlation matrix $\mathbf{R}_{\mathrm{LL}}$, which contains the inter-correlations between 18 land-cover type fraction vectors $\boldsymbol{f_L}$. R_S is equivalent to the maximum correlation (Pearson's r^2) between the spatial variability of C state/process variable $\mathbf{c}_S$ and the best-fitting linear combination of land-cover type fractions $\mathbf{f}_L$. The resulting R_S values are shown in Fig. 6 (main text).

We also employ a multiple correlation coefficient analysis on the empirical orthogonal functions (EOFs, or the "primary modes" of variability) of all $\boldsymbol{c_s}$. We conducted a principal component analysis to derive the eight primary EOFs (EOFs were derived using "pca.m" function in Matlab; each $\boldsymbol{c_s}$ vector is centered at zero and scaled to the standard deviation of $\boldsymbol{c_s}$). Standardized EOFs (normalized by EOF standard deviation) and EOF coefficients are shown in Fig. S4. The EOF maps exhibit the primary modes of $\boldsymbol{c_s}$ variability in space; for each $\boldsymbol{c_s}$, the maximum spatial variability explained by EOFs 1 – N is the sum of standardized EOFs 1 – N multiplied by their associated coefficients. EOF multiple correlation coefficients – $R_{S(EOF)}$ – were derived for the primary two, four and eight EOFs based on equation 9, where R_{LL} is the identity matrix (as EOFs are orthogonal). $R_{S(EOF)}$ results are shown in Fig. 6 in the main text.

S7 Comparison against the MsTMIP terrestrial biosphere model ensemble

We compare GPP, ecosystem respiration and NCE against the MsTMIP terrestrial biosphere model ensemble Version 1.0 (64) net C exchange (note: total C exchange reported as net ecosystem exchange, or 'NEE', by MsTMIP). The 0.5° × 0.5° monthly GPP, total (heterotrophic and autotrophic) respiration and NCE values for 2001-10 – based on the BG1 simulation – were downloaded from (http://nacp.ornl.gov/mstmipdata/), and were aggregated to a 1° × 1° grid (the BG1 simulation includes time-varying nitrogen deposition, atmospheric CO_2 and land-use history (22)). The eight MsTMIP models shown in Fig. S5 are BIOME-BGC, CLASS-CTEM-N, CLM4VIC, CLM4, DLEM, ISAM, TEM6, TRIPLEX-GHG (for the sake of brevity, we did not label each individual MsTMIP model in Fig. S5);

S8 Atmospheric CO_2 comparison

We incorporated the 2009-2010 CARDAMOM monthly mode net C exchange (NCE) values into the GEOS-Chem atmospheric chemistry and transport model (29). The GEOS-Chem model simulations are based on GEOS-Chem version 8.2, driven by NASA GEOS-5 meteorological fields. In addition to NCE, fossil fuel emissions and oceanic surface CO_2 fluxes are prescribed (56). We compared the 2009-2010 GEOS-Chem model CO_2 concentrations against the monthly mean anomaly across 12 Total Carbon Column Observing Network sites (TCCON, 38): Bialystok, Poland; Darwin, Australia; Eureka, Canada; Garmisch, Germany; Karlsruhe, Germany; Lauder, New Zealand; Lauder, New Zealand; Lamont, Oklahoma; Orleans, France; Park Falls, Wisconsin; Sodankyla, Finland; Wollongong, Australia. Details of the GEOS-Chem TCCON comparison are reported by (63) and references therein. We note that the uncertainty in the GEOS-Chem trend

due to CARDAMOM flux uncertainty is substantial: global NCE 25^{th} – 75^{th} percentile = -8 – +13Pg C yr^{-1}, which roughly corresponds to a ±5ppm growth rate (1). To evaluate the CARDAMOM seasonal NCE variability, we compare the linearly de-trended model and observations (Fig. S6).

Figures

Fig. S1: Left two columns: posterior GPP C allocation to autotrophic respiration (equivalent to 1 – C use efficiency), labile C, foliar C, fine roots, wood (mean, left column) and associated uncertainty (standard deviation, right column). **Middle two columns:** Posterior C residence time in foliar C, fine roots, wood, litter and soil C (log-based mean, left column) and associated uncertainty factors (based on logarithmic standard deviation, right column). **Right two columns:** Posterior mean 2001-10 C stocks in labile, foliar, fine roots, wood, litter C pools (mean, left column) and associated uncertainties (standard deviation, right column).

Fig. S2. Posterior median and 50% confidence ranges shown for 1° × 1° grid-cells B, T, D and W shown for the unperturbed results (S0) and sensitivity experiments S1-S12. The coordinates of B, T, D and W are reported in the Materials and Methods (locations shown in inset map). Across all locations, 88% of median sensitivity analysis estimates (sensitivity tests S1-S12) are within ±50% of unperturbed median C state and process variable retrievals.

Fig. S3. Pearson correlation coefficients (r^2, shown in color bar) between GLOBCOVER land-cover types fractions (x-axis) and C state and process variables (y-axis), based on their correlation across all 1° × 1° grid cells within the global study area. See section S5 for land-cover type acronyms.

Fig. S4: Maps: Eight primary 1° × 1° standardized empirical orthogonal functions (EOFs 1-8) derived from a principal component analysis of standardized C state and process variables (see section S6). The two dominant modes (EOF1 and EOF2) together reflect first-order global variations in C state/process variables ($\boldsymbol{c}_s$) due to in latitude and precipitation, while higher order modes reflect increasingly complex spatial structures (however, EOFs 3-8 typically account for a smaller portion of $\boldsymbol{c}_s$ spatial variability). **Scatter plots:** standardized EOF 1-8 coefficients corresponding to each C state/process variable (shown as symbol-color combinations). The linear sum of standardized EOFs 1-4 (1-8) and their associated coefficients reproduces 29-95% (88-99%) of C state/process variability (see Fig. 6 in the main text).

Fig. S5: CARDAMOM zonal profiles of median gross primary production, ecosystem respiration, fires and net C exchange (red). The 50% confidence range is depicted as a light-pink shaded area. The blue lines represent the 8 global MsTMIP models (64; see section S7 for details). The dashed black line denotes the flux-tower derived GPP (36). The continuous black line denotes the GFED version 3 total C emissions (36).

Fig. S6. 2009-2010 GEOS-Chem model - with CARDAMOM mode NCE - compared against mean monthly TCCON atmospheric column measurements across 12 TCCON sites: the left panel shows atmospheric CO_2 concentrations, and the right panel shows the linearly de-trended CO_2 anomalies. The de-trended comparison Pearson's r = 0.93 and RMSE = 0.53 ppm.

Tables

Table S1: DALEC2 parameters, descriptions and prior ranges (the DALEC2 equations are fully described in (35)).

Table S2: Sensitivity tests for C allocation, residence times and C pool size estimates at locations B, T, D and W.

Table S3: In-situ observations and CARDAMOM posterior state and process variable estimates.

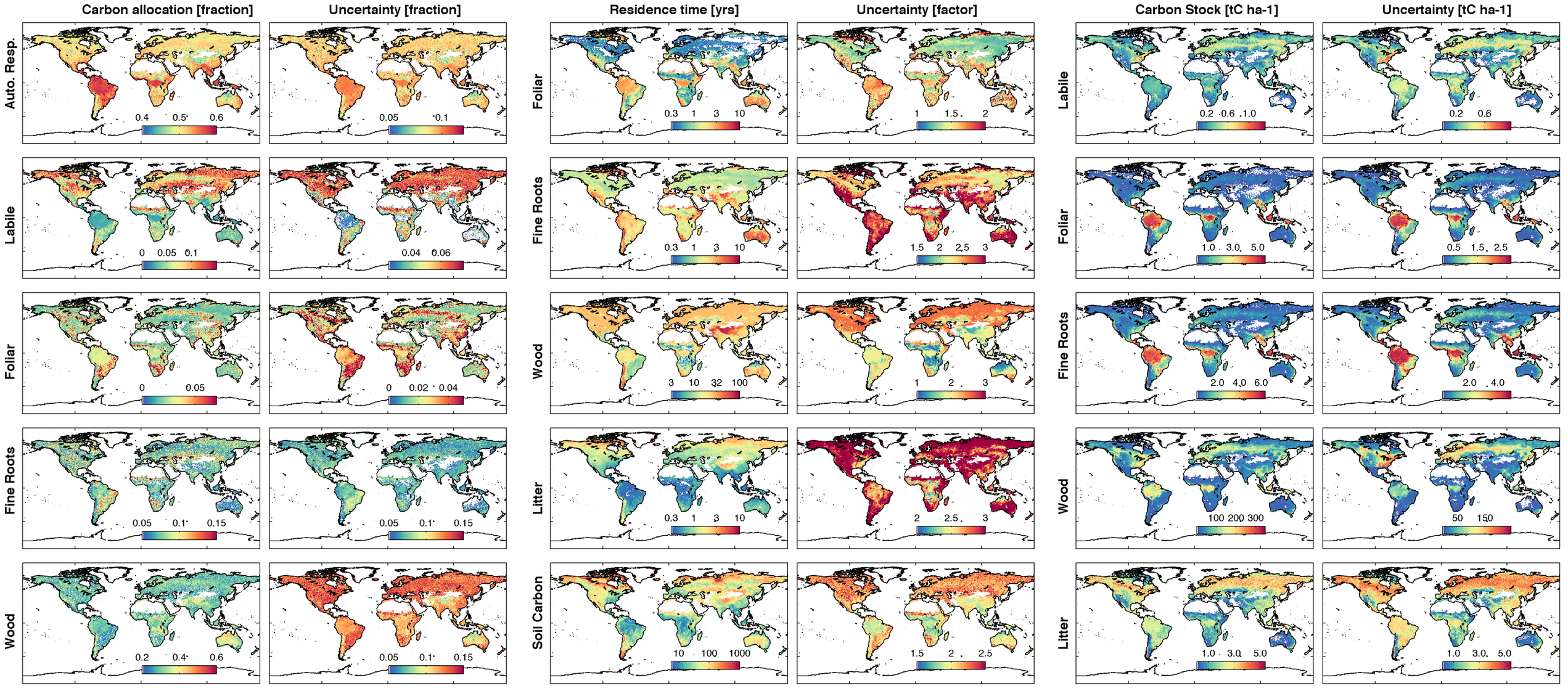
Carbon allocation [fraction]
Uncertainty [fraction]
Residence time [yrs]
Uncertainty [factor]
Carbon Stock [tC ha-1]
Uncertainty [tC ha-1]
Auto. Resp.
Labile
Foliar
Fine Roots
Wood
Foliar
Fine Roots
Wood
Litter
Soil Carbon
Labile
Foliar
Fine Roots
Wood
Litter
0.4 0.5 0.6
0.05 0.1
0.3 1 3 10
1 1.5 2
0.2 0.6 1.0
0.2 0.6
0 0.05 0.1
0.04 0.06
1.5 2 2.5 3
1.0 3.0 5.0
0.5 1.5 2.5
0 0.05
0 0.02 0.04
3 10 32 100
1 2 3
2.0 4.0 6.0
2.0 4.0
0.05 0.1 0.15
0.05 0.1 0.15
2 2.5 3
100 200 300
50 150
0.2 0.4 0.6
0.05 0.1 0.15
10 100 1000
1.5 2 2.5
1.0 3.0 5.0
1.0 3.0 5.0

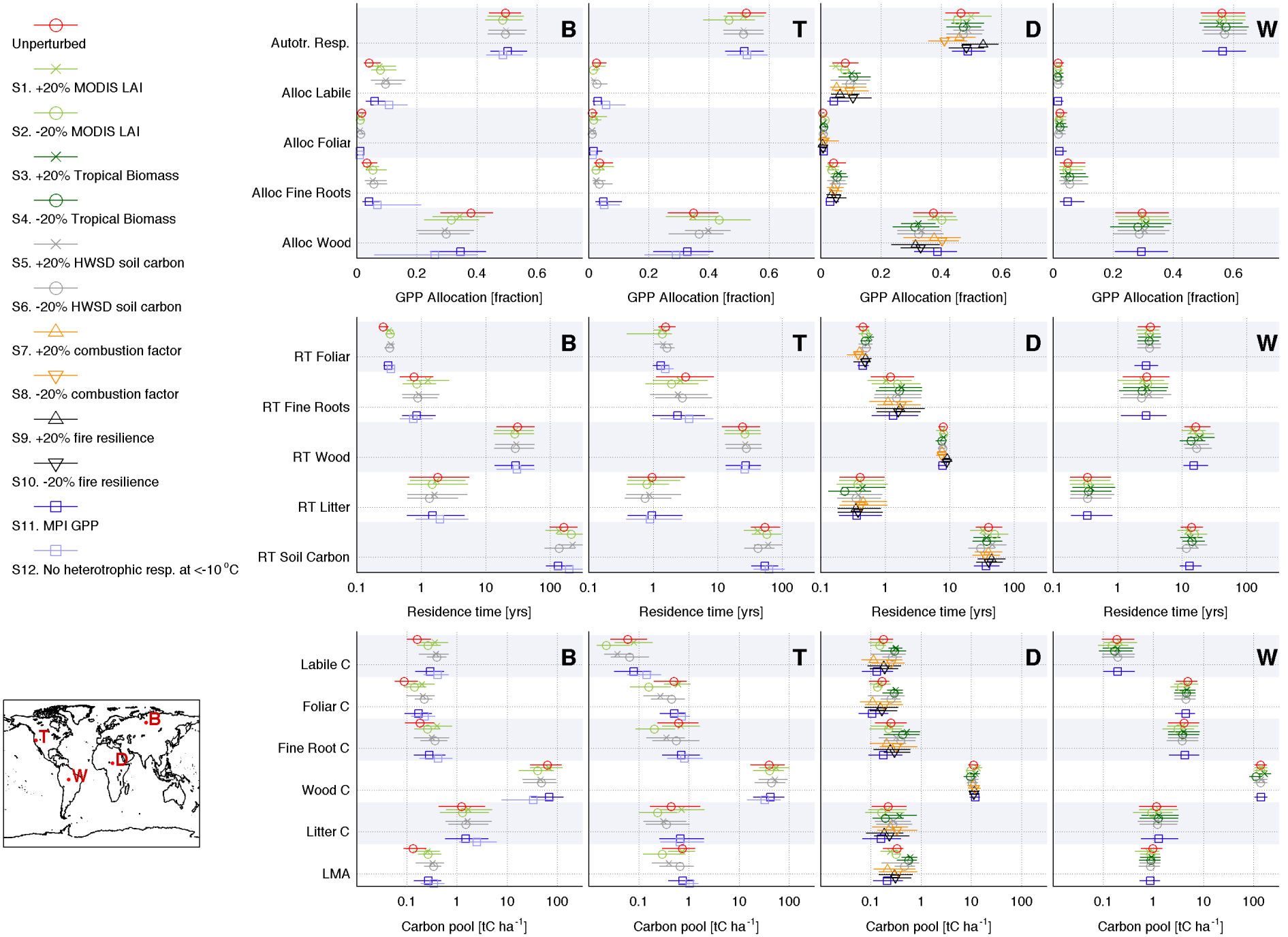
Unperturbed
S1. +20% MODIS LAI
S2. -20% MODIS LAI
S3. +20% Tropical Biomass
S4. -20% Tropical Biomass
S5. +20% HWSD soil carbon
S6. -20% HWSD soil carbon
S7. +20% combustion factor
S8. -20% combustion factor
S9. +20% fire resilience
S10. -20% fire resilience
S11. MPI GPP
S12. No heterotrophic resp. at <-10 °C
B
T
D
W
Autotr. Resp.
Alloc Labile
Alloc Foliar
Alloc Fine Roots
Alloc Wood
GPP Allocation [fraction]
RT Foliar
RT Fine Roots
RT Wood
RT Litter
RT Soil Carbon
Residence time [yrs]
Labile C
Foliar C
Fine Root C
Wood C
Litter C
LMA
Carbon pool [tC ha-1]

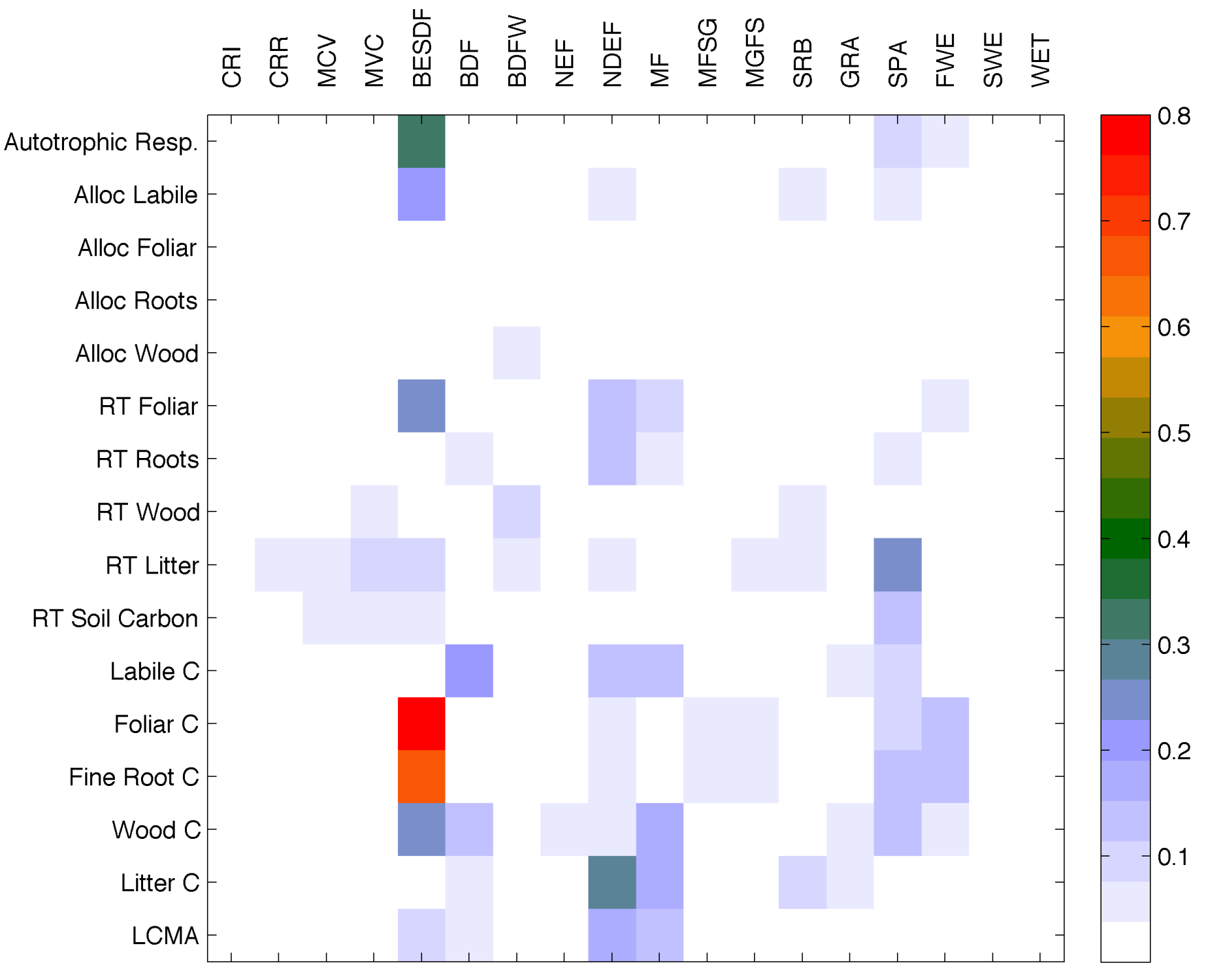
CRI
CRR
MCV
MVC
BESDF
BDF
BDFW
NEF
NDEF
MF
MFSG
MGFS
SRB
GRA
SPA
FWE
SWE
WET
Autotrophic Resp.
Alloc Labile
Alloc Foliar
Alloc Roots
Alloc Wood
RT Foliar
RT Roots
RT Wood
RT Litter
RT Soil Carbon
Labile C
Foliar C
Fine Root C
Wood C
Litter C
LCMA
0.8
0.7
0.6
0.5
0.4
0.3
0.2
0.1

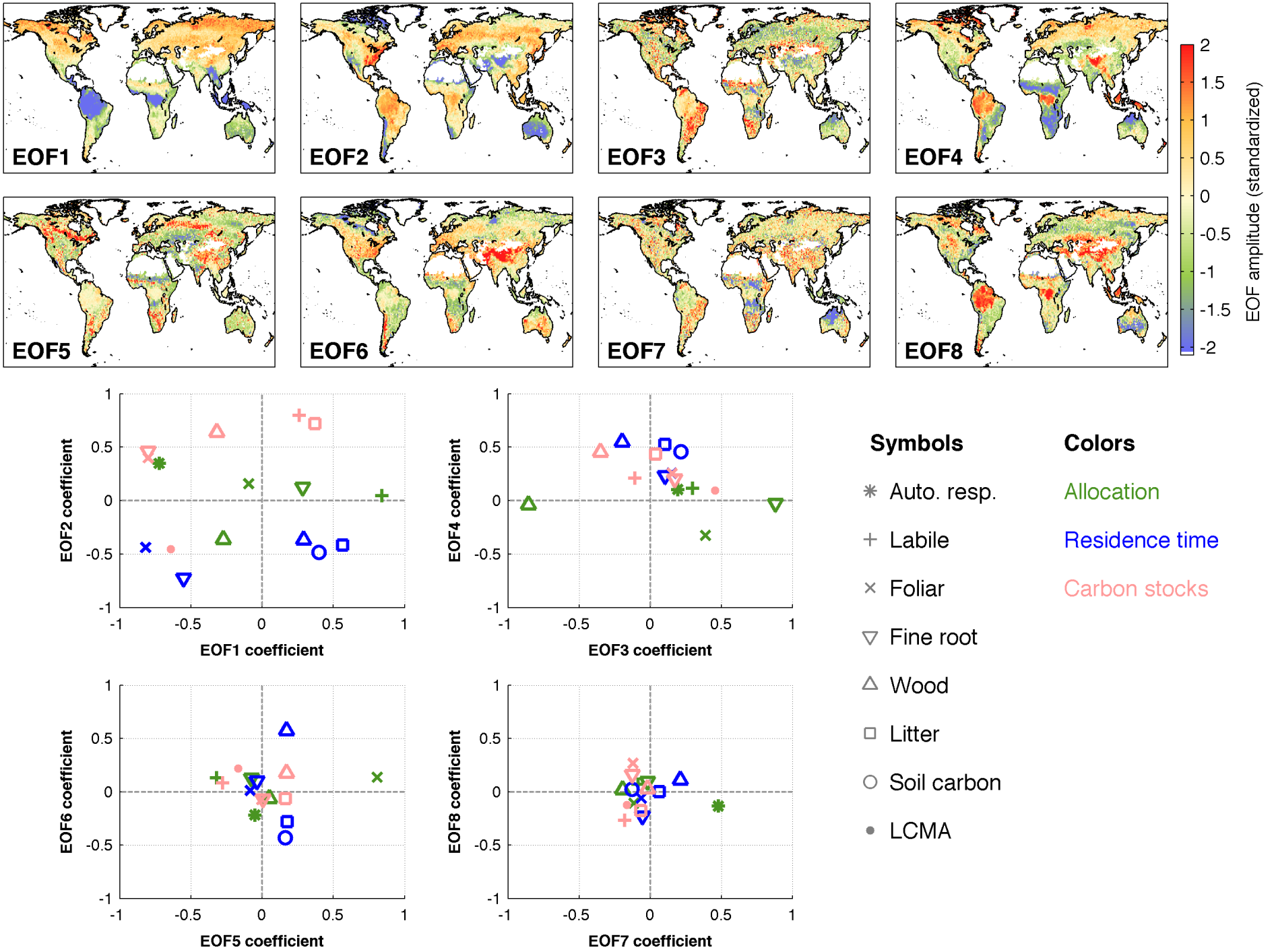
EOF1
EOF2
EOF3
EOF4
EOF5
EOF6
EOF7
EOF8
EOF amplitude (standardized)
2
1.5
1
0.5
0
-0.5
-1
-1.5
-2
EOF2 coefficient
EOF1 coefficient
EOF4 coefficient
EOF3 coefficient
EOF6 coefficient
EOF5 coefficient
EOF8 coefficient
EOF7 coefficient
Symbols
Auto. resp.
Labile
Foliar
Fine root
Wood
Litter
Soil carbon
LCMA
Colors
Allocation
Residence time
Carbon stocks

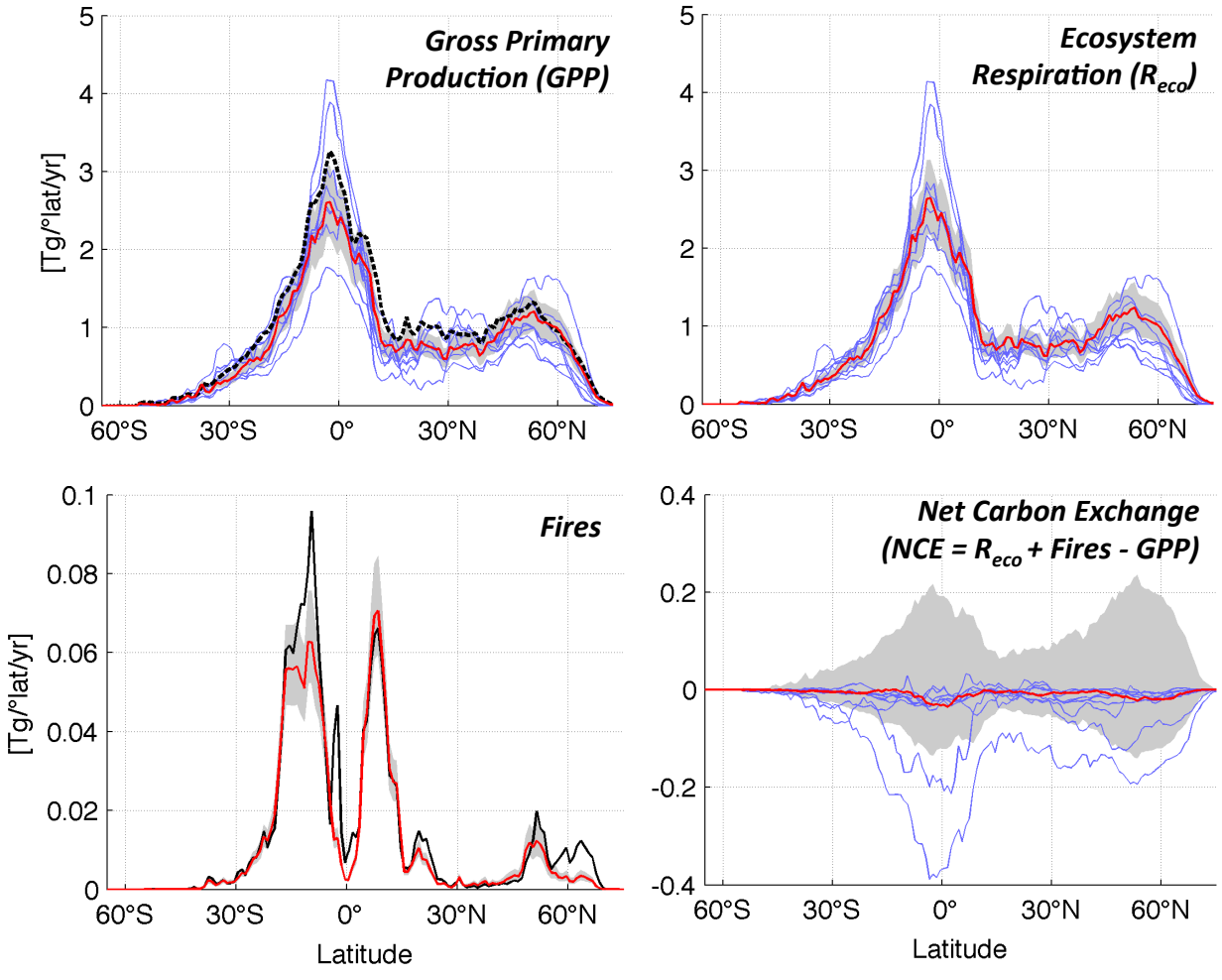

CARDAMOM
median (mode for NCE)

CARDAMOM
50% C.R.

FLUXNET derived GPP
Jung et al., 2009

MsTMIP models
Huntzinger et al., 2013.

GFEDv3
van der Werf et al., 2010

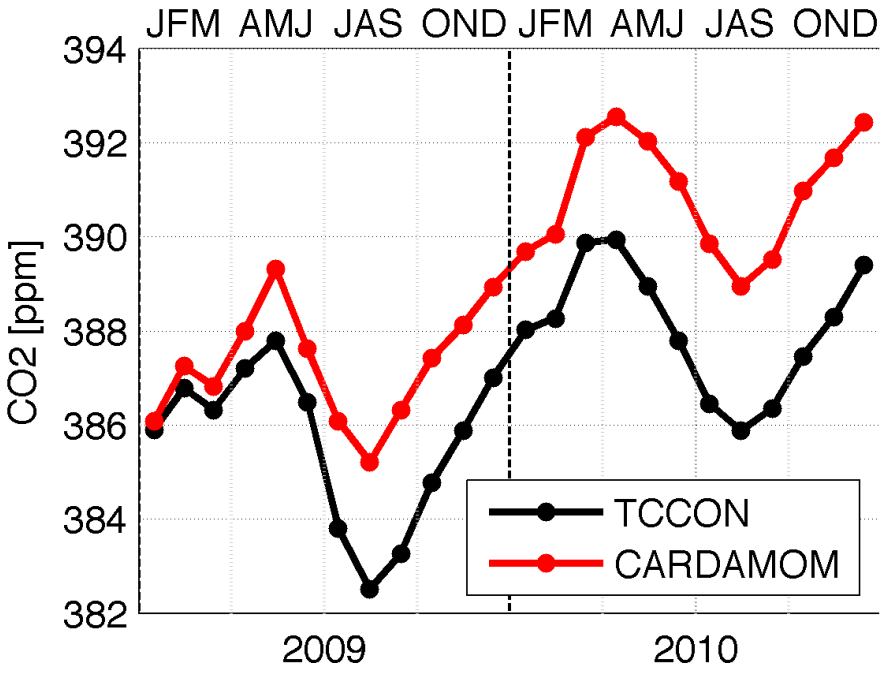
JFM AMJ JAS OND JFM AMJ JAS OND
394
392
390
388
386
384
382
CO2 [ppm]
TCCON
CARDAMOM
2009
2010

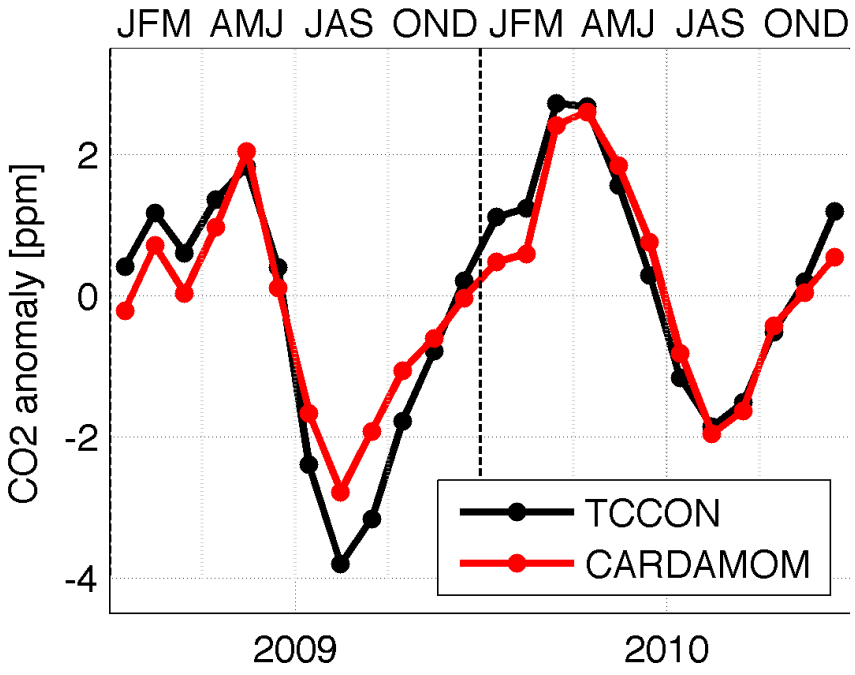
JFM AMJ JAS OND JFM AMJ JAS OND
2
0
-2
-4
CO2 anomaly [ppm]
TCCON
CARDAMOM
2009
2010

Table S1: DALEC2 parameters, descriptions and prior ranges (the DALEC2 equations are fully described in (35)).

	Parameters	**Prior Range**
Allocation fractions	Autotrophic Respiration	0.2-0.8*
	Labile	0.01-0.5
	Foliage	0.01-0.5
	Fine roots	0.01-0.5
	Wood	0.01-0.5
Turnover rates	Woody C turnover rate	2.5×10^{-5} –10^{-3} d^{-1}
	Fine root turnover rate	10^{-4} –10^{-2} d^{-1}
	Litter turnover rate	10^{-4} –10^{-2} d^{-1}
	Soil organic C turnover rate	10^{-7} –10^{-3} d^{-1}
	Litter mineralization rate	10^{-2} –10^{-5} d^{-1}
	Exponential temperature dependence	0.018–0.08
Canopy parameters	Leaf onset day	1-365.25
	Leaf fall day	1-365.25
	Canopy efficiency	5 – 50*
	Leaf C mass per leaf area (LCMA)	5 - 200 gC m^{-2}
	Annual leaf loss fraction	1/8 – 1
	Labile C release period	10 – 100 days
	Leaf fall period	20 – 150 days
Initial C stocks	Labile C	1-2000gC m^{-2}
	Foliar C	1-2000gC m^{-2}
	Fine root C	1-2000gC m^{-2}
	Litter C	1-2000gC m^{-2}
	Above & Below ground wood	1 - 100,000gC m^{-2}
	Soil C (1m depth)	1 - 200,000gC m^{-2}

***** Autotrophic Respiration and Canopy efficiency parameter log-normal prior distributions are described in section S1.

Table S2: Sensitivity tests for C allocation, residence times and C pool size estimates at locations B, T, D and W.

Sensitivity Test(s)	**Description**
S1 & S2	+20% & -20% in LAI observations
S3 & S4	+20% & -20% increase in biomass observations
S5 & S6	+20% & -20% increase in HWSD Soil Carbon observations
S7 & S8	+20%[1] & -20% increase in fire combustion factors
S9 & S10	+20% & -20% increase in fire resilience factor
S11	Use mean 1° × 1° aggregated MPI GPP (36) as driver
S12	No heterotrophic respiration[2] under -10°C

[1]Foliar combustion factor increase by 10% (from 0.9 to 0.99).

[2]Respiration temperature dependence coefficient (19) set to zero at <-10°C, scaled by unity at >0°C, and scaled from 0 to 1 between -10°C and 0°C.

Table S3: In-situ observations and CARDAMOM posterior state and process variable estimates.

Measurement (region)	**CARDAMOM range**[*]	**In-situ observations (study)**
Fine roots (Amazon river basin)	9.2 – 10.8 tC ha^{-1} (2.8 – 11.5 tC ha^{-1})	5 – 8 tC[**] $ha^{-1(a)}$ (65)
Fine roots (North-East U.S.; >30°N, >100°W)	1.6 – 3.3 tC ha^{-1} (0.9 – 6.0 tC ha^{-1})	1.25 tC[**] $ha^{-1(a)}$ (66)
Fine root residence time (North-East U.S., >30°N, >100°W)	1.1 – 1.5 yrs (0.9 – 3.2 yrs)	0.83 – 1.25 $yrs^{(a)}$ (66)
Fine root RT (global: where woody C > 10tC ha^{-1})	1.2 – 2.6 yrs (0.9 – 4.7 yrs)	1.25 – 2.5 $yrs^{(b)}$ (67)
Wood Carbon RT (Amazon river basin)	15 – 21 yrs (9 – 24 yrs)	~20 – 70$yrs^{(b)}$ (20, above-ground only)
Carbon Use Efficiency (CUE)[***] (Amazon river basin)	0.42 – 0.43 (0.42 – 0.45)	Amazon field sites: 0.32 – 0.47[(b)] (39)
Fine root C (Lat > 66°N)	0.3 – 0.4 tC ha^{-1} (0.2 – 0.6 tC ha^{-1})	Arctic Ecosystems: 0.1 – 5 tC $ha^{-1(b)}$ (68)

[*]Area-weighted 25th – 75th %ile (5th – 95th %ile) 1° × 1° C state and process variables (see Materials and Methods).

[**]Dry mass to C mass conversion factor = 0.5

[***]CUE = 1 – autotrophic respiration fraction

[a]Individual site range

[b]regional or global range